International Journal of Nanomedicine

Dovepress
Taylor & Francis Group

Open Access Full Text Article

ORIGINAL RESEARCH

Harnessing a cRGD-Targeted Schottky Junction MXene Nanocomposite for Potent Bladder Cancer Therapy: Dual-Modal PTT/PDT Effects with Immune Activation and Favorable Comparison to Doxorubicin

Zhibo Gu, Hua Zhu, Yong Zhang, Jie Jiang, Donghua Gu, Jiangang Chen

Department of Urology, Nantong First People's Hospital, Affiliated with Southeast University, Nantong, Jiangsu, 226200, People's Republic of China

Correspondence: Jiangang Chen, Department of Urology, Nantong First People's Hospital, Affiliated with Southeast University, No. 666 Victory Road, Chongchuan District, Nantong, Jiangsu, 226200, People's Republic of China, Tel +8621 15996558081, Email urologistcjg@163.com

Objective: This study developed a multifunctional $MnFe_2O_4$/$TiVNbMoC_3$-cRGD (MXenes) nanocomposite for targeted photothermal- photodynamic therapy against bladder cancer.

Methods: A multifunctional MXene-based nanocomposite was constructed by integrating $MnFe_2O_4$ nanoparticles onto $TiVNbMoC_3$ MXene nanosheets to form a layer-on-layer Schottky junction, followed by conjugation of cRGD peptides for tumor targeting. Successful synthesis, colloidal stability, broad optical absorption, efficient photothermal conversion and ROS generation under 808 nm laser were confirmed. In vitro assays were conducted using 5637 bladder cancer cells, and a murine bladder tumor model was established to evaluate the anticancer efficacy. Biocompatibility assessments were also carried out.

Results: The composite was constructed by integrating $MnFe_2O_4$ nanoparticles onto $TiVNbMoC_3$ MXene nanosheets, which formed a layer - on - layer Schottky junction. Then, cRGD peptides were conjugated to the surface for tumor targeting. Comprehensive characterization confirmed successful synthesis, favorable colloidal stability, broad optical absorption, and efficient photothermal conversion and reactive oxygen species (ROS) generation under 808 nm laser irradiation. In vitro, the cRGD-targeted nanocomposite was efficiently internalized by 5637 bladder cancer cells and showed significantly higher anticancer efficacy than doxorubicin (DOX), including inhibition of proliferation, migration, colony formation, and induction of apoptosis and immunogenic cell death. In a murine bladder tumor model, the nanocomposite achieved the strongest tumor growth suppression and reduced final tumor volume more effectively than DOX. Biocompatibility assessments showed minimal hemolysis and no major organ damage at therapeutic doses.

Conclusion: This MXene-based Schottky junction nanocomposite represents a promising targeted platform for dual-modal photothermal/photodynamic therapy combined with immune activation in bladder cancer, warranting further translational investigation.

Keywords: bladder cancer, Schottky junction, semiconductor nanocatalysts, multimodal treatment, targeted therapy

Introduction

Bladder cancer is the sixth most common cancer in men, accounting for ~6% of new cancer cases.[1] Current standard treatments (surgery and chemotherapy) improve early-stage survival but have major limitations: a 40–50% overtreatment rate, a formidable five-year recurrence rate of 50–70%, and an inherent risk of risk of progression to muscle invasive disease.[2] Thus, these modalities often prove insufficient to prevent disease recurrence and progression, frequently compromising patients' long-term quality of life. There is, an urgent clinical need for more effective strategies.

In this context, novel treatment modalities such as photodynamic therapy (PDT), photothermal therapy (PTT), chemodynamic therapy (CDT), and immunotherapy have emerged as promising alternatives or complements to conventional oncology regimens.[3–5] These approaches offer distinct mechanisms of action and can be engineered to act synergistically, making

https://doi.org/10.2147/IJN.S597220
Received: 8 March 2026
Accepted: 9 June 2026
Published: 12 June 2026

Graphical Abstract

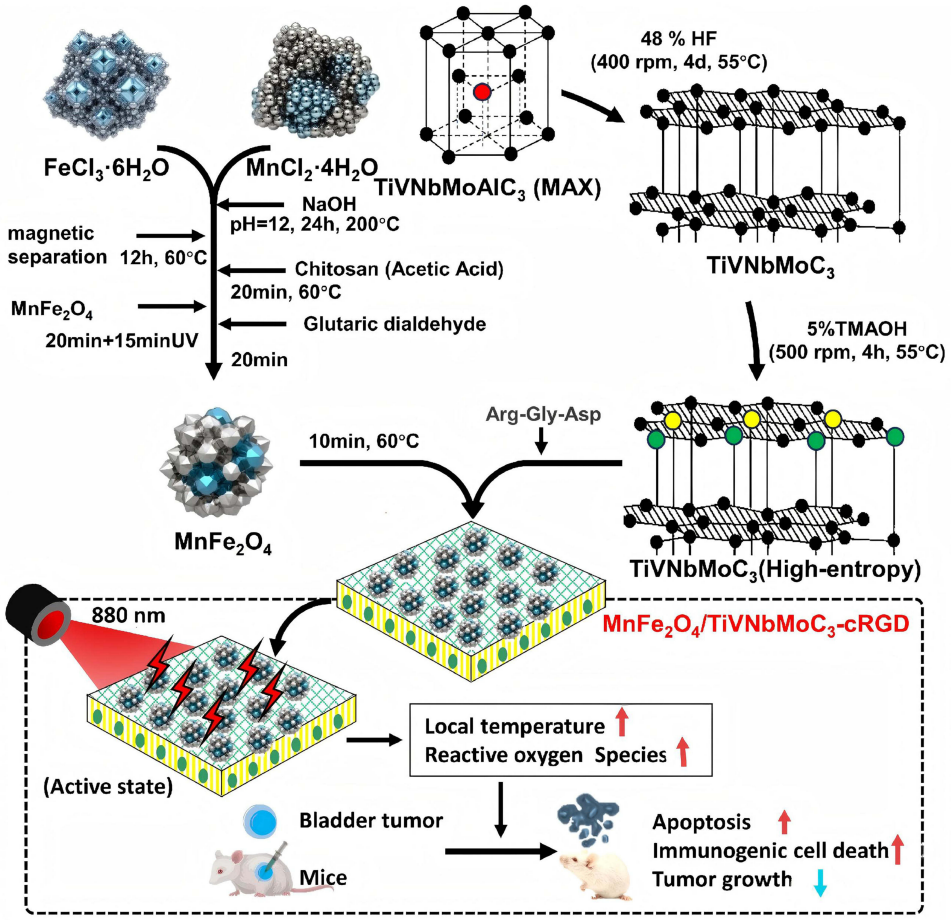

multimodal combination therapy a pivotal strategy capable of producing superior therapeutic outcomes often exemplifying a remarkable "1+1>2" effect-compared to monotherapies or their simple superposition.[6,7] For instance, in bladder cancer, Chen et al[8] enhanced bladder cancer therapy by combining PTT with glucose fueled CDT and GSH depletion to remodel the TME.

Nanotechnology provides a powerful toolkit to rationally design and implement such synergistic strategies. Schottky junction nanocatalysts (metal-semiconductor interfaces) efficiently manage photogenerated charge carriers.[9] Their catalytic reactions mechanism involves: (i) light induced electron-hole pair generation, (ii) charge separation driven by the Schottky barriers built in electric field (suppressing recombination),[10] and (iii) surface reactions generating cytotoxic reactive oxygen species (ROS).[11] ROS bursts trigger immunogenic cell death (ICD), releasing tumor antigens and damage-associated molecular patterns to initiate adaptive immunity.[12] This principle has succeeded in type II heterojunctions and Au@CuS nanoparticles.[13,14] Furthermore, Chen H. et al[15] optimized an MXene@TiO_2/Fe_3O_4 Schottky platform for exosome based bladder cancer detection.

Given ongoing challenges of drug resistance and off target toxicity, integrating the unique advantages of Schottky junction nanocatalysts into the therapeutic paradigm presents a compelling avenue.[16] A nanocatalyst leveraging accelerated photoelectrodynamic processes could achieve precise tumor eradication while mitigating conventional treatment drawbacks.[5] This study develops such a Schottky junction based nanocatalytic platform and rigorously evaluates its efficacy against bladder cancer.

Methods and Materials

Synthesis and Characterization

Synthesis of $TiVNbMoC_3$ MXene

$TiVNbMoC_3$ MXene was synthesized by selectively etching the aluminum layer from the $TiVNbMoAlC_3$MAX phase. Specifically, the MAX powder was added to 50 mL of 48 wt% hydrofluoric acid (HF) and continuously stirred at 55 °C and 400 rpm for 4 days. The resulting mixture was then washed repeatedly with deionized water via centrifugation (4000 rpm, 3–5 min per cycle) until the supernatant reached a neutral pH (6–7). The sediment was subsequently treated with 5 wt% tetramethylammonium hydroxide (TMAOH) and stirred at 55 °C for 4 h to achieve delamination. Finally, the single-layer MXene nanosheets were collected from the supernatant and obtained by freeze-drying. (The MAX precursor and etching reagents were sourced from Beike Nanotechnology Co., Ltd., Suzhou, China).

Synthesis of $MnFe_2O_4$ Nanoparticles

$MnFe_2O_4$ nanoparticles were prepared via a hydrothermal method. First, 0.495 g (2.5 mmol) of $MnCl_2{\cdot}4H_2O$ (Aladdin Biochemical Technology Co., Ltd., Shanghai, China) was dissolved in 40 mL of an aqueous solution containing 1.35 g (5 mmol) of $FeCl_3{\cdot}6H_2O$ under stirring for 1 h. A predetermined volume of NaOH solution was then added dropwise until a black precipitate formed. The mixture was transferred into a Teflon-lined stainless-steel autoclave and heated at 200 °C for 24 h. After cooling, the product was collected by centrifugation, washed alternately with deionized water and ethanol, and dried in an oven at 60 °C for 12 hours.

Fabrication of MXenes Nanocomposite

To prepare the final nanocomposite, a chitosan solution was first prepared by dissolving 0.5 g of chitosan in 100 mL of 2% glacial acetic acid with stirring at 65 °C for 20 minutes. Then, 0.1 g of the as-synthesized $MnFe_2O_4$ nanoparticles and 10 mL of a $TiVNbMoC_3$ MXene aqueous dispersion (10 mg/mL) were added to the chitosan solution. The mixture was stirred at 60 °C for 10 minutes and then allowed to stand overnight. The resulting product, $MnFe_2O_4$/$TiVNbMoC_3$, was collected by centrifugation, washed several times with distilled water, and freeze-dried. Finally, cRGD peptides were immobilized onto the nanocomposite surface via π-π stacking and electrostatic interactions to form MXenes, which was stored at 4 °C for subsequent use. The resulting structure features a layer-on-layer Schottky junction.

Stability and Storage

Synthesis and handling: All MXene synthesis and exfoliation steps are carried out under argon atmosphere in a glovebox to minimize oxygen exposure. Storage: The as-prepared $TiVNbMoC_3$ MXene nanosheets are lyophilized and stored as a powder under vacuum at −20°C in amber vials. For colloidal dispersions, the MXene is freshly dispersed in deoxygenated deionized water or PBS (pH ~7.4) immediately before use. Stability validation: We regularly characterize the material by XPS to monitor surface oxidation (eg, TixOy formation) and UV-vis-NIR to track the characteristic absorption peak. Typically, the material remains stable for at least one week under these conditions. Transport: For inter-laboratory transport, the powder is sealed under argon in a double-layered vial with desiccant and shipped on dry ice.

Colloidal Characterization

Colloidal stability was evaluated via the Tyndall effect. Briefly, 800 μL of the nanocomposite suspension and 800 μL of PBS (control) were separately placed in Eppendorf tubes. A laser pointer was used to irradiate each tube. A clear visible beam path in the nanocomposite suspension, absent in the PBS control, indicated good dispersibility and colloidal stability.

Detection of ROS

ROS generation was measured using 1,3-diphenylisobenzofuran (DPBF) as a probe. First, 1.2 mL of $MnFe_2O_4$ /$TiVNbMoC_3$ solution (100 μg/mL) and PBS control was mixed with 10 μL of DPBF ethanolic solution (100 μM). The mixture was transferred to a quartz cuvette and irradiated with an 808 nm laser (1 W/cm^2). The decomposition of DPBF was monitored by recording the decrease in absorbance at 410 nm at 1-min intervals for 7-min.

Photothermal Performance Measurement with 808 nm Laser

The photothermal performance of the nanocomposite was evaluated under 808 nm near-infrared (NIR) laser irradiation. The material's aqueous dispersions and pure water (control) were placed in separate vessels. Temperature changes were monitored in real-time using an infrared thermal camera.

In vitro Cellular Assays

Cell Culture

Human bladder cancer 5637 cells (C6018, Beyotime Biotechnology Co., Ltd., China) were cultured in Dulbecco's Modified Eagle Medium (DMEM, Thermo Fisher Scientific, USA) supplemented with 10% fetal bovine serum. Cells were maintained at 37 °C in a humidified atmosphere containing 5% CO_2.

Cell Viability Assay

Cell viability was assessed using the Cell Counting Kit8 (CCK-8, C0038, Beyotime). Cells were seeded in 96-well plates at approximately 60% confluence and treated with various concentrations of nanomaterials ($TiVNbMoC_3$, $MnFe_2O_4$ /$TiVNbMoC_3$ and $MnFe_2O_4$/ TiVNbMo C_3-RGD) for 48 h under 808 nm laser irradiation. Thereafter, CCK-8 reagent was added to each well and incubated at 37 °C for 1 h. Absorbance was measured at 450 nm using a microplate reader. Cell viability was calculated as follows: Cell Viability (%) = [(OD_Experimental − OD_Blank) / (OD_Control − OD_Blank)] × 100.

Cellular Uptake

Cells grown on coverslips were treated with the nanocomposite (25 μg/mL) for 0, 2, 4, 8, or 12 h. After treatment, cells were washed with PBS and further cultured for 24 h. Cell membranes were labeled with DiO (green fluorescence, C1038, Beyotime) by incubation at 37 °C for 60 min, and nuclei were stained with DAPI (blue fluorescence, C1006, Beyotime) for 5 min. The intracellular localization of the Cy5.5-labeled nanocomposite (red fluorescence) was visualized using confocal laser scanning microscopy. Co-localization with membrane (green) and nuclear (blue) signals was analyzed to evaluate uptake efficiency and time dependence.

Cytotoxicity Assay (Calcein AM/PI Staining)

Cytotoxicity was evaluated using a Calcein AM/PI Cell Viability/Cytotoxicity Assay Kit. Cells were seeded in a 24-well plate at ~60% confluence and treated with nanomaterials (50 μg/mL) for 48 hours. Following treatment, the cells were washed with PBS and further cultured in complete medium for 24 hours. The culture medium was then removed, and the cells were washed once with PBS before being incubated with an appropriate volume of the Calcein AM/PI working solution for 30 minutes at 37°C. After incubation, aspirate the solution and wash the cells three times with pre-warmed culture medium. Staining was visualized under a fluorescence microscope, with Calcein AM (green fluorescence, Ex/Em=494/517 nm) indicating live cells and PI (red fluorescence, Ex/Em=535/617 nm) indicating dead cells.

Colony Formation Assay

Cells were seeded into 6-well plates at an initial density of 60%. After treatment with the nanomaterials (25 μg/mL), the cells were cultured until visible colonies had formed. The culture medium was then removed, and the cells were gently washed with PBS, fixed with 4% paraformaldehyde for 20 min, and stained with crystal violet for another 20 min. Following a final PBS wash and air-drying, the colonies were photographed and counted to evaluate the long-term proliferative capacity and clonogenic survival of the cells.

Scratch Wound Healing Assay

Cell migration was assessed using a scratch wound healing assay. Cells were seeded in a 6-well plate at 60% confluence and treated with nanomaterials (25 μg/mL) for 48 hours. After treatment, the cells were washed with PBS and cultured in serum-free medium for 6 hours. A straight scratch was then gently created across the cell monolayer using a sterile pipette tip. The initial wound (0 hours) was imaged under an inverted microscope. The cells continued to be cultured in serum-free medium for another 48 hours, after which the same locations were re-imaged to assess wound closure.

Apoptosis Assay

Cell apoptosis was analyzed using an Annexin V-APC Apoptosis Detection Kit by flow cytometry. Cells were seeded in a 6-well plate at 60% confluence and treated with nanomaterials (50 μg/mL) for 48 hours. After treatment, the adherent cells were washed with PBS, detached using trypsin, and collected by centrifugation at 1000 rpm for 5 minutes. The cell pellet was gently resuspended in PBS and counted. Subsequently, 100,000 cells were centrifuged again, resuspended in Annexin V-binding buffer (AP107 MultiSciences Biotech Co., Ltd), and stained with 10 μL of propidium iodide (PI) solution (C2015M, Beyotime Co., Ltd). The cells were incubated at room temperature (20–25°C) in the dark for 10 minutes. Finally, the samples were placed on ice and immediately analyzed by flow cytometry.

Western Blot Analysis

Bladder cancer cells were treated according to different experimental groups different experimental groups (PBS control, $TiVNbMoC_3$ group, DOX group (0.2uM), $MnFe_2O_4$/ $TiVNbMoC_3$ -RGD + 808 nm laser irradiation (1.0 W/cm^2, 10 min) group). Proteins were extracted using RIPA lysis buffer containing protease inhibitors. Protein concentration was determined with a BCA assay. Equal amounts of protein were separated by SDS-PAGE and transferred onto PVDF membranes. Membranes were blocked with 5% skim milk and incubated overnight at 4 °Cwith primary antibodies against high-mobility group box 1 (HMGB1, 10,829-1-AP), calreticulin,(CRT, 27298-1-AP), and GAPDH (14751-1-AP; all from Sanying Biotechnology Co., Ltd., Wuhan, China). After incubation with HRP-conjugated secondary antibodies, protein bands were visualized using an ECL substrate and quantified by densitometry, with GAPDH as the loading control.

In vivo Antitumor Efficacy and Biosafety Evaluation

Establishment of Bladder Tumor Model and Treatment Protocol

All animal procedures followed the National Institutes of Health guidelines and were approved by the Animal Ethics Committee of Nantong University (Approval No. S20251225-001). Male BALB/c mice (4–6 weeks old, weighing 18–22 g) were were inoculated subcutaneously with 5×10^6 5637 bladder cancer cells in the right flank. When tumors reached approximately 50 mm^3 (around day 7 post inoculation), mice were randomly assigned into four treatment groups (n = 5 per group): (1) PBS control, (2) $TiVNbMoC_3$MXene only (100 μg/mL), (3) DOX (2 mg/kg, intraperitoneal injection every 2 days), (4) $MnFe_2O_4$/$TiVNbMoC_3$- cRGD nanocomposite (100 μg/mL, intratumoral injection) + 808 nm laser irradiation (1.0 W/cm^2, 10 min). The sample size (n = 5 per group) was determined based on a power analysis assuming a medium effect size (Cohen's d = 0.8), $\alpha = 0.05$ (two-tailed test), and a desired power of 80%, which yielded a minimum requirement of 5 mice per group, consistent with previously published guidelines for preclinical tumor xenograft models.[17] Tumor volumes were measured every 3 days using a digital caliper and calculated as V = (length × width^2)/2. The experimenter performing tumor measurements was blinded to group allocation. At the end of the study (day 14), mice were euthanized, and tumors and major organs were harvested for further analysis.

Immunohistochemical Analysis of Tumor Tissues

TUNEL Staining for Apoptosis Detection

Tumor tissue sections were deparaffinized in xylene, rehydrated through a graded ethanol series, and rinsed with PBS. After permeabilization with Proteinase K (20 μg/mL, ST535, Beyotime) for 20 min at room temperature and washing, then sections were equilibrated with 1x Equilibration Buffer for 10–30 min. The TdT reaction mixture was then applied, and slides were incubated at 37 °C for 60 min in a humidified chamber. Following a PBS wash, nuclei were counter-stained with DAPI (2 μg/mL, C1006, Beyotime) for 5 min at RT. After a final wash, slides were immediately imaged under a fluorescence microscope (TUNEL signal: 520±20 nm; DAPI: 460 nm).

Ki-67 Immunofluorescence Staining for Proliferation Assessment

We evaluated tumor proliferation by staining for the Ki-67 antigen. Following deparaffinization and rehydration, tissue sections underwent antigen retrieval. After blocking the non-specific binding sites, the tissue sections were incubated with an anti - Ki - 67 primary antibody (1:200, AG2646, Beyotime) overnight at 4 °C. After washing, a fluorescently

labeled secondary antibody was applied. Nuclei were counterstained with DAPI, and slides were imaged using a fluorescence microscope. Parallel sections were stained with hematoxylin and eosin (H&E) for general histopathological evaluation.

Biosafety Evaluation

Hemolysis Assay

The hemolysis assay was performed as follows. First, red blood cells (RBCs) were isolated from 1 mL of human whole blood. The blood was diluted with 2 mL of 1x PBS and centrifuged at 500 g for 10 minutes; this purification step was repeated five times. Subsequently, the isolated RBCs were adjusted to a concentration of 2.5×10^6 cells mL^{-1} using 1x PBS. To obtain six final concentrations (5–200 μg mL^{-1}), 200 μL of this RBC suspension was added to 800 μL of the Schottky junction composite suspension for the test. All mixtures, along with positive (deionized water) and negative (1xPBS) controls, were incubated at 37°C for 3 hours on a shaker. Following incubation, the samples were centrifuged at 10,050 rpm for 5 minutes, and the hemoglobin release was quantified by measuring the absorbance of the supernatant at 540 nm.

Histopathological Analysis of Major Organs

To assess systemic toxicity, we harvested major organs (heart, liver, spleen, lungs, and kidneys) were harvested from tumor-bearing mice at the endpoint of the study. Tissues were fixed in 10% neutral buffered formalin, embedded in paraffin, and sectioned at 4 μm thickness. Sections were stained with H&E and examined under a light microscope for any signs of histopathological abnormality.

Results

Synthesis and Characterization of $MnFe_2O_4$/$TiVNbMoC_3$ Nanozyme

The $MnFe_2O_4$/$TiVNbMoC_3$ nanozyme was successfully synthesized, as outlined in Scheme 1. Its morphology was examined by scanning electron microscopy (SEM, Figure 1A) and transmission electron microscopy (TEM, Figure 1B). As shown, $TiVNbMoC_3$ serves as a substrate, forming a uniform matrix on which $MnFe_2O_4$/$TiVNbMoC_3$ nanoparticles are evenly deposited. High-magnification images (Figure 2) reveal no significant phase separation or large-scale agglomeration, confirming the successful formation of a well-integrated composite.

Energy-dispersive X-ray spectroscopy (EDX) verified the elemental composition (Figure 3). A representative EDX spectrum of the material was shown. Peaks corresponding to the constituent elements of $TiVNbMoC_3$MXene (Ti, V, Nb, Mo, C) alongside Fe from $MnFe_2O_4$ are clearly detected. The C-K and O-K peaks appear in the low-energy region (<1 keV), while the Ti-K, V-K, Fe-K, and a potential Cu-K peak (possibly from the sample holder) are located at approximately 4.5 keV, 5 keV, 6.4 keV, and 8 keV, respectively. The Mn peak remains unidentified, likely due to its weak signal or overlap with neighboring peaks. The oxygen content may originate from both the $MnFe_2O_4$ lattice and potential surface oxidation. The pronounced carbon peak stems primarily from the MXene backbone. No significant impurity peaks were detected, supporting the successful synthesis of the target composite.

The crystalline structure was analyzed by X-ray diffraction (XRD) (Figure 4). The diffraction pattern of $TiVNbMoC_3$ showed characteristic peaks at $2\theta \approx 36°$, 41°, and 74°. New peaks emerging at approximately 30°, 35°, and 62° correspond to the characteristic reflections of MnFe2O4, confirming its successful incorporation into the composite.

Dynamic light scattering (DLS) indicated an average hydrodynamic diameter of approximately 165 nm (Figure 5A), consistent with TEM observations. The material exhibited a zeta potential of −27.9 mV (Figure 5B), confirming good colloidal stability in aqueous dispersion. This stability was further corroborated by a distinct Tyndall effect (Figure 6), where a laser beam passed through the dispersion produced a visible light-scattering path, characteristic of a stable colloid.

Surface chemical states were investigated by X-ray photoelectron spectroscopy (XPS). The survey scan spectrum of the material showed all detected elements (Figure 7A). (B-I) High- resolution XPS spectra of C 1s (Figure 7B), Fe 2p (Figure 7C), Mo3d (Figure 7D), Nb 3d (Figure 7E), V 2p (Figure 7F), O1s (Figure 7G) and Mn 2p (Figure 7H) and Ti 2p (Figure 7I) regions. The high-resolution spectra revealed the following: C 1s: Deconvoluted into C–C (284.8 eV), C–O, and C=O bonds. Fe 2p: The Fe 2p peak at ~711 eV is indicative of Fe^{3+}, consistent with its state in MnFe2O4.Nb 3d: The Nb $3d_5$/peak at ~207 eV suggests

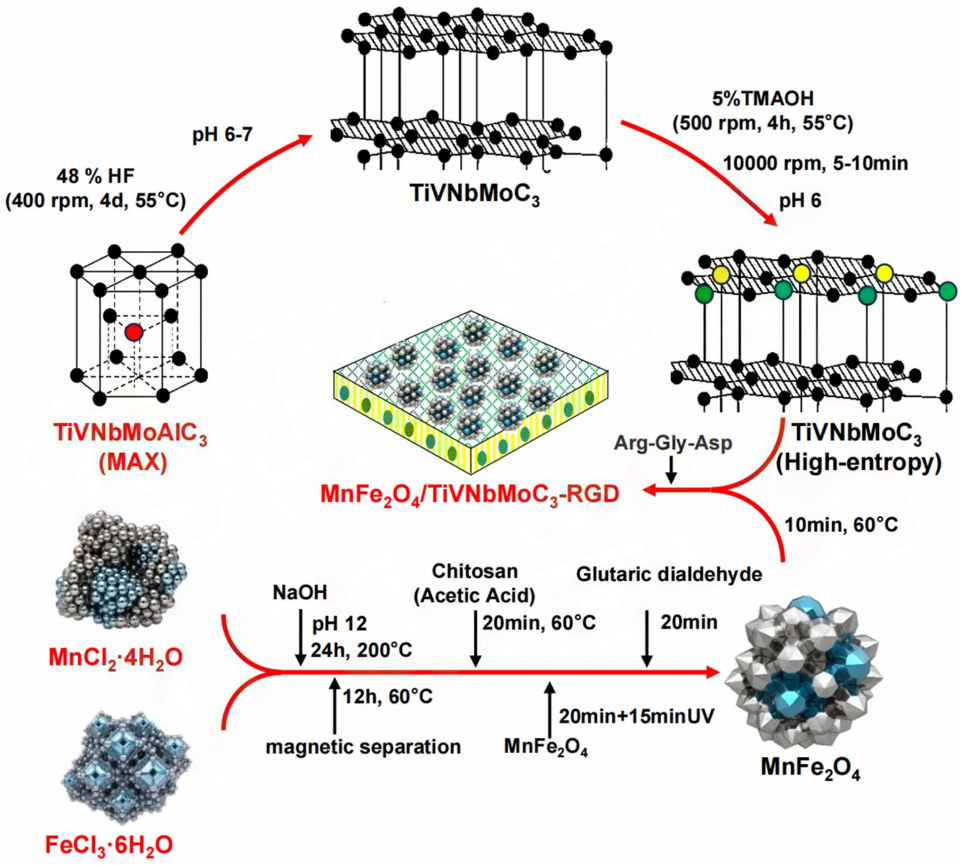

Scheme 1 Synthesis and Characterizations of the Schottky Junction Semiconductor Nanocatalysts $MnFe_2O_4$/ $TiVNbMoC_3$.

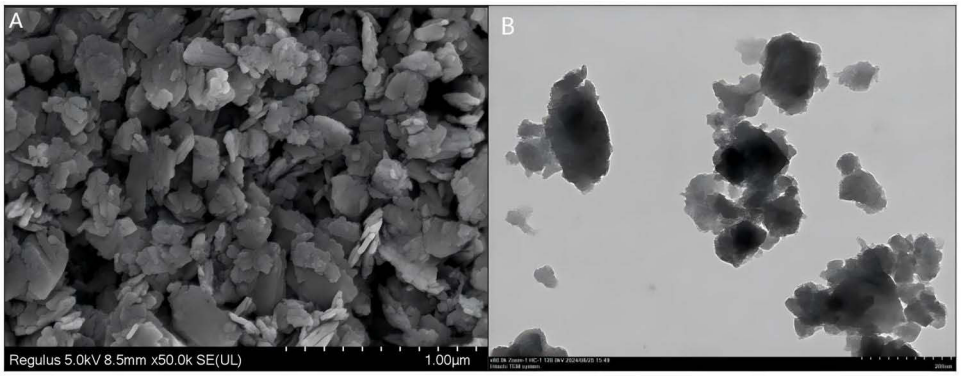

Figure 1 (**A**) SEM image of $MnFe_2O_4$/$TiVNbMoC_3$ composite material. $MnFe_2O_4$ adhere to the surface of $TiVNbMoC_3$ lamellar layers, manifesting as clusters of aggregated particles due to its magnetic properties. (**B**) TEM image of the composite of $TiVNbMoC_3$ monolayer and $MnFe_2O_4$ nanoparticles. The dark areas in the image represent $MnFe_2O_4$, which is clearly bound to the surface of the $TiVNbMoC_3$ monolayer, indicating successful synthesis of the composite material.

a high oxidation state (Nb).V 2p: The V $2p_3$/peak position (~516–517 eV) corresponds to V or V.O 1s: Comprised contributions from lattice oxygen (~530 eV) and surface-adsorbed oxygen/hydroxyl groups (~531–532 eV). Mn 2p: The characteristic doublet indicates the presence of mixed $Mn^{2+}$and Mn^{3+}oxidation states. Ti 2p: The Ti 2p/ peak at ~458–459 eV confirms Ti exists primarily as $Ti.^{4+}$

https://doi.org/10.2147/IJN.S597220

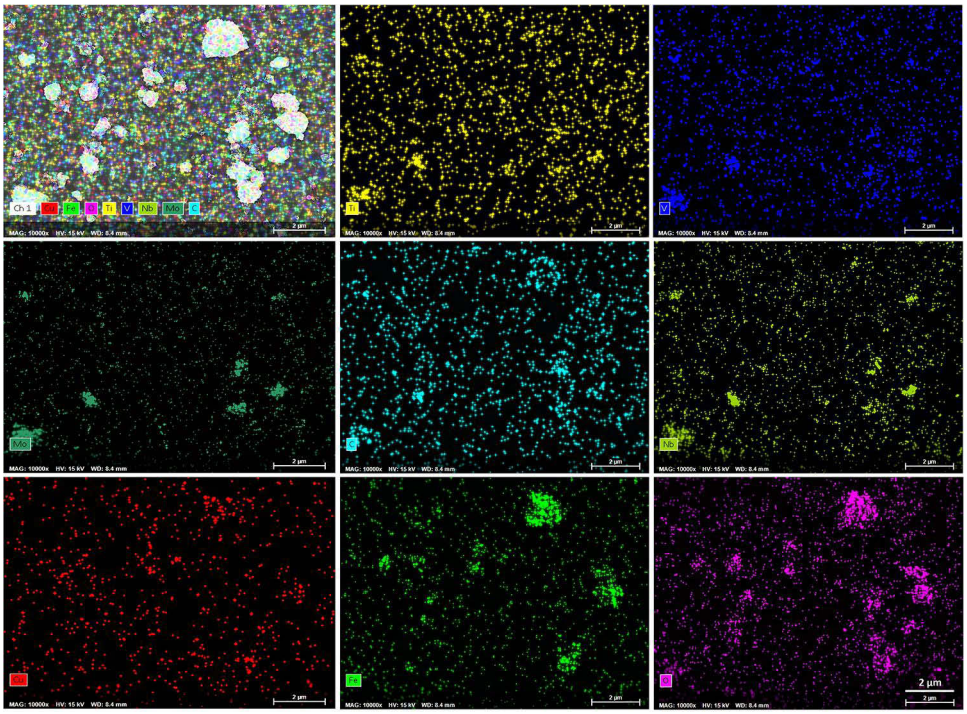

Figure 2 The distribution of Mn (dark green) and Fe (light green) elements closely overlaps, confirming the formation of $MnFe_2O_4$. The distribution of oxygen (pink) is somewhat correlated with that of Mn and Fe, but it is also present in other regions, potentially indicating partial oxidation on the sample surface.

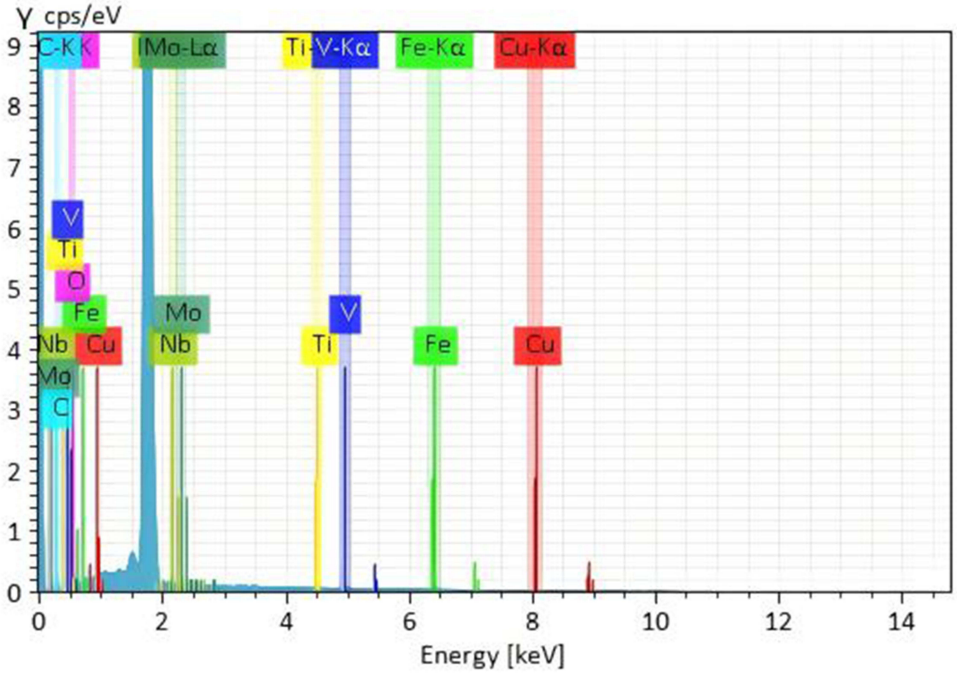

Figure 3 Energy-dispersive X-ray spectroscopy (EDX) elemental analysis of the $MnFe_2O_4$ /$TiVNbMoC_3$ nanocomposite.

Optical and Functional Properties

UV–vis spectroscopy was used to evaluate optical absorption (Figure 8). The $MnFe_2O_4$/$TiVNbMoC_3$ composite exhibited broad absorption from 300 to 800 nm. Compared to pure $TiVNbMoC_3$, the UV absorption intensity of the

 https://doi.org/10.2147/IJN.S597220

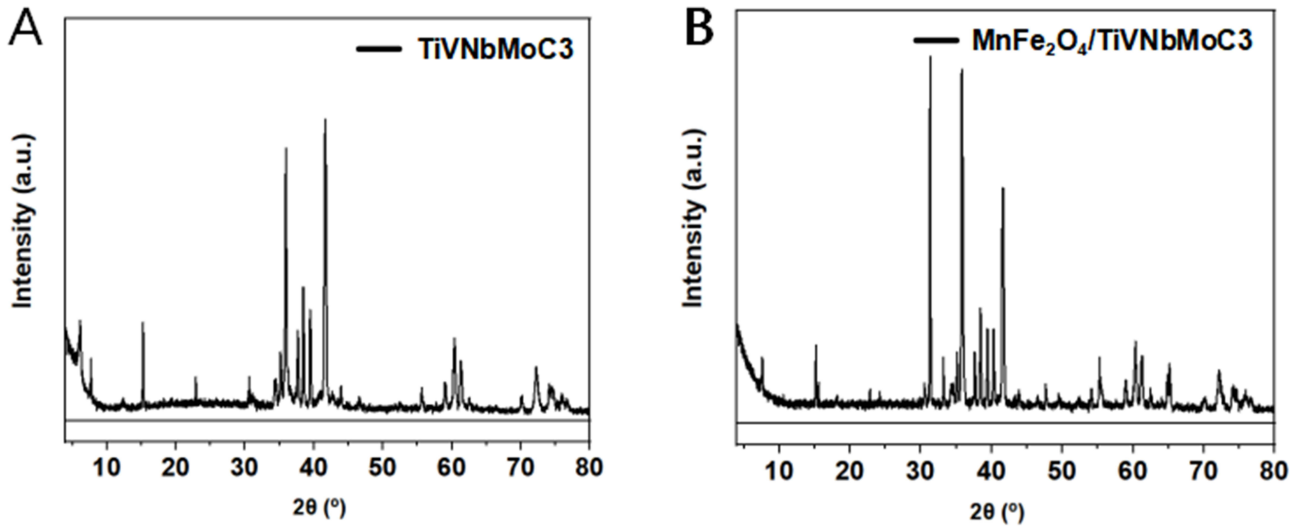

Figure 4 XRD reveals the primary diffraction peaks of the $TiVNbMoC_3$ (**A**) and $MnFe_2O_4$ /$TiVNbMoC_3$ (**B**).

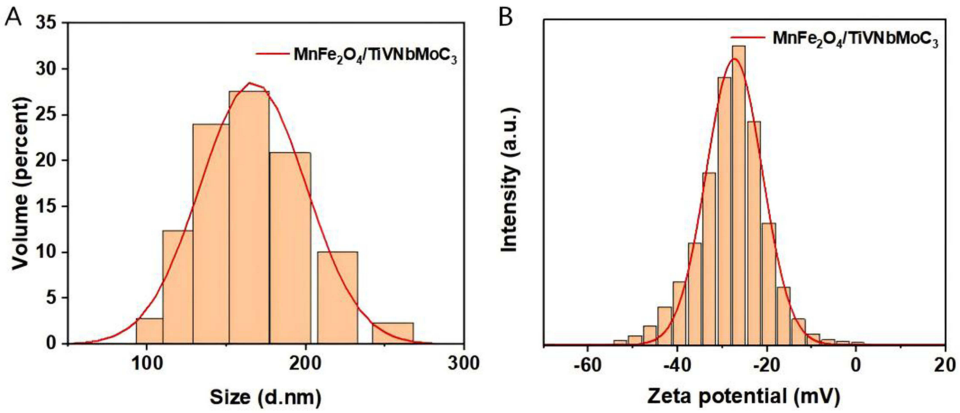

Figure 5 Hydrodynamic diameter and zeta potential characterization of the $MnFe_2O_4$/ TiVNb MoC_3 -RGD nanocomposite. (**A**) Size distribution profile measured by dynamic light scattering (DLS). The peak indicates an average hydrodynamic diameter of approximately 165 nm (**A**). (**B**) Zeta potential measurement (**B**). The average zeta potential of the material in PBS buffer was −27.9 mV, indicating a negatively charged surface and confirming good colloidal stability.

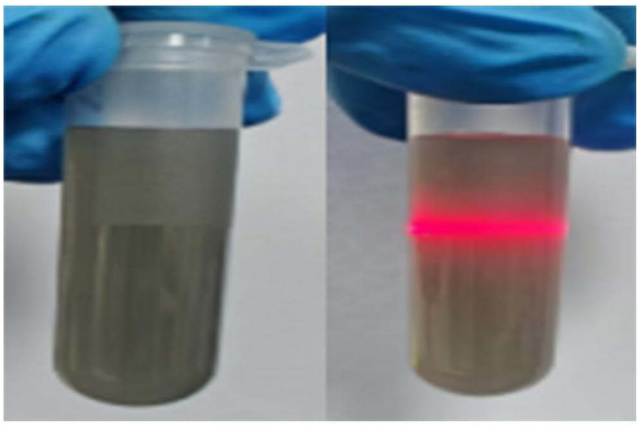

Figure 6 Tyndall effect.

https://doi.org/10.2147/IJN.S597220

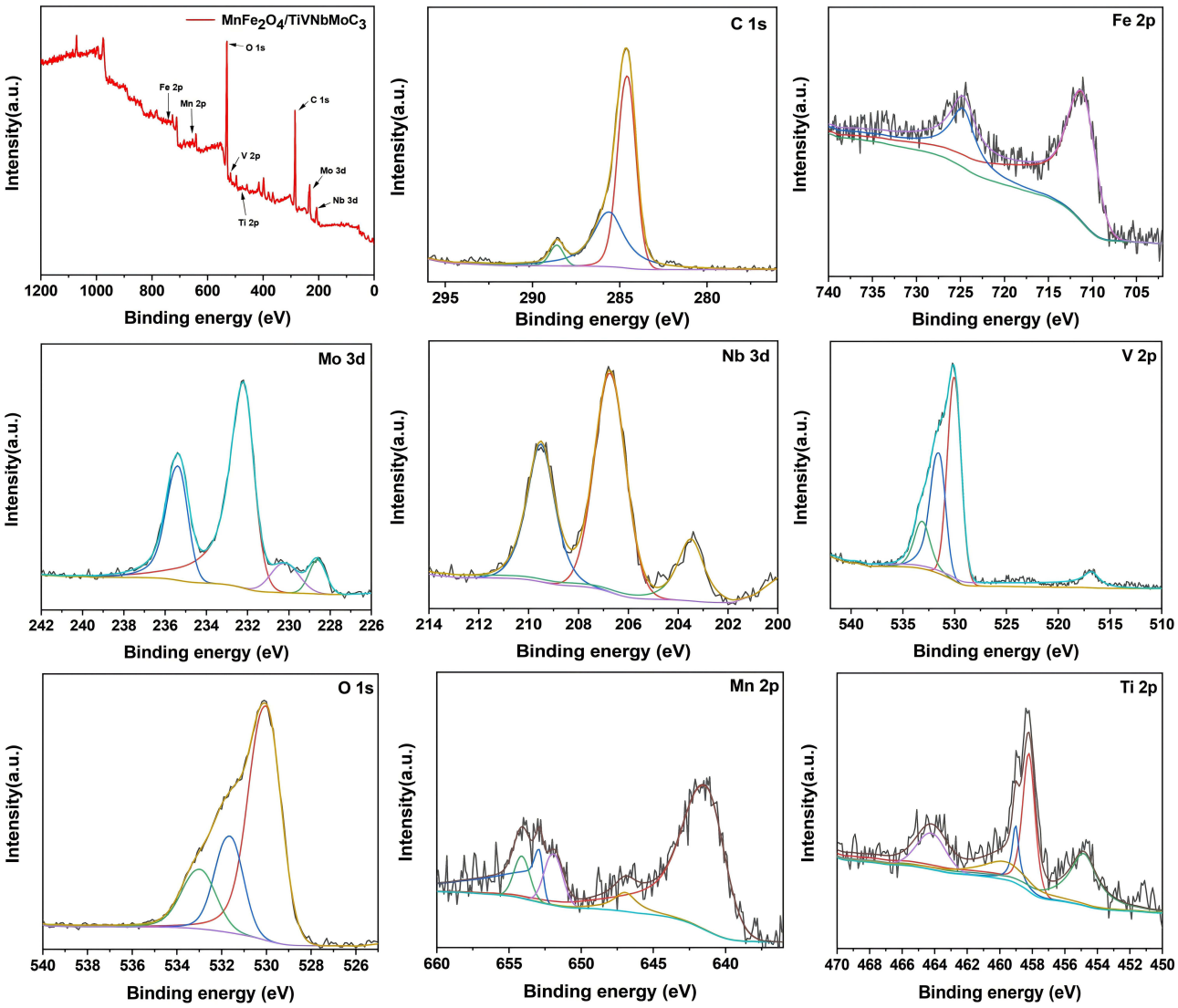

Figure 7 X-ray photoelectron spectroscopy (XPS) characterization and surface chemical state analysis of the $MnFe_2O_4$/ $TiVNbMoC_3$ -RGD nanocomposite. The survey scan spectrum of the material showed all detected elements (**A**). (**B–I**) High- resolution XPS spectra of C 1s (**B**), Fe 2p (**C**), Mo3d (**D**), Nb 3d (**E**), V 2p (**F**), O1s (**G**) and Mn 2p (**H**) and Ti 2p (**I**) regions.

composite decreased, but it showed significantly enhanced absorption in the visible to near - infrared region (400–800 nm) due to the incorporation of $MnFe_2O_4$.

The reactive oxygen species (ROS) generation capability was assessed with 1,3-diphenylisobenzofuran (DPBF) as a probe. Under light irradiation, the characteristic absorption of DPBF at 410 nm decreased progressively over time for the composite dispersion, indicating continuous ROS production. In contrast, no significant change was observed in the PBS control (Figure 9).

The photothermal performance was evaluated under 808 nm NIR laser irradiation (Figure 10). An aqueous dispersion of the nanocomposite exhibited a rapid temperature increase, reaching approximately 42 °C within 25 minutes, significantly higher than the minimal temperature change observed for pure water. This demonstrates the material's effective photothermal conversion capability.

 https://doi.org/10.2147/IJN.S597220

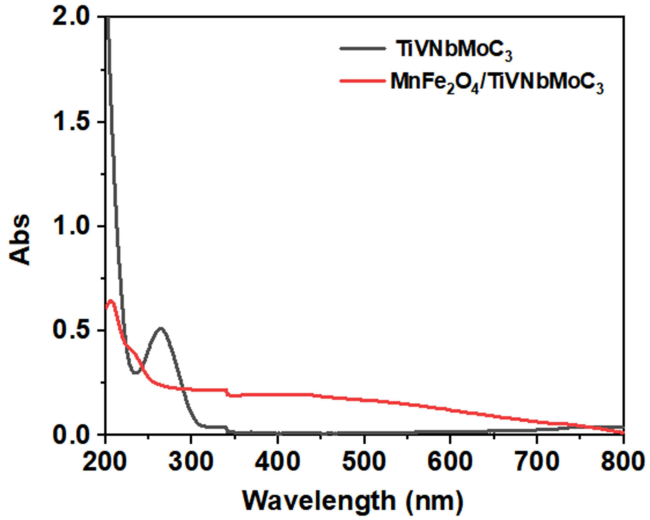

Figure 8 Optical absorption properties of the nanocomposite.

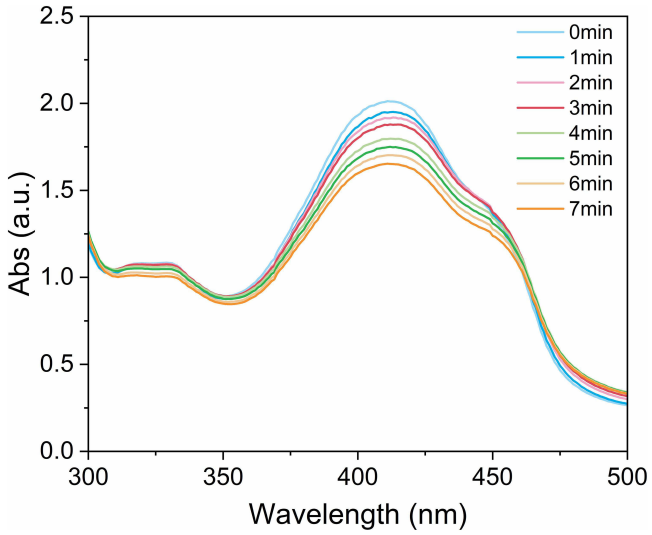

Figure 9 ROS generation capacity of the nanocomposite under 808 nm laser irradiation measured using the DPBF probe method. Time-dependent decrease (0–7 min) in the characteristic absorbance of DPBF at 410 nm, indicating the ROS generation kinetics of the $MnFe_2O_4$/ $TiVNbMoC_3$ -RGD composite (100 μg/mL) and control groups under 808 nm laser irradiation (1 W/cm^2).

In vitro Cellular Assays

Cellular Uptake and Localization

Over time, the red fluorescence (Cy5.5) gradually increased from nearly undetectable at 0 h to markedly enhanced at 12 h, indicating time-dependent accumulation of the material inside the cells. The green fluorescence (DiO) remained relatively stable throughout the process, clearly delineating the cell membrane structure. The blue fluorescence (DAPI) showed that the nucleus position remained largely unchanged. In the merged images, an increasing colocalization of red and green fluorescence was observed over time, suggesting progressive internalization of the material by the cells.

These results demonstrate that the nanocomposite is efficiently taken up by bladder cancer cells in a time-dependent manner, supporting its potential for therapeutic applications. The cellular internalization of the Cy5.5-labeled $MnFe_2O_4$/$TiVNbMoC_3$-RGD nanocomposite was tracked over time using confocal microscopy (Figure 11). The red fluorescence signal (Cy5.5) was nearly undetectable at 0 h and then increased progressively, indicating continuous cellular accumulation. At 12 h, a strong

https://doi.org/10.2147/IJN.S597220

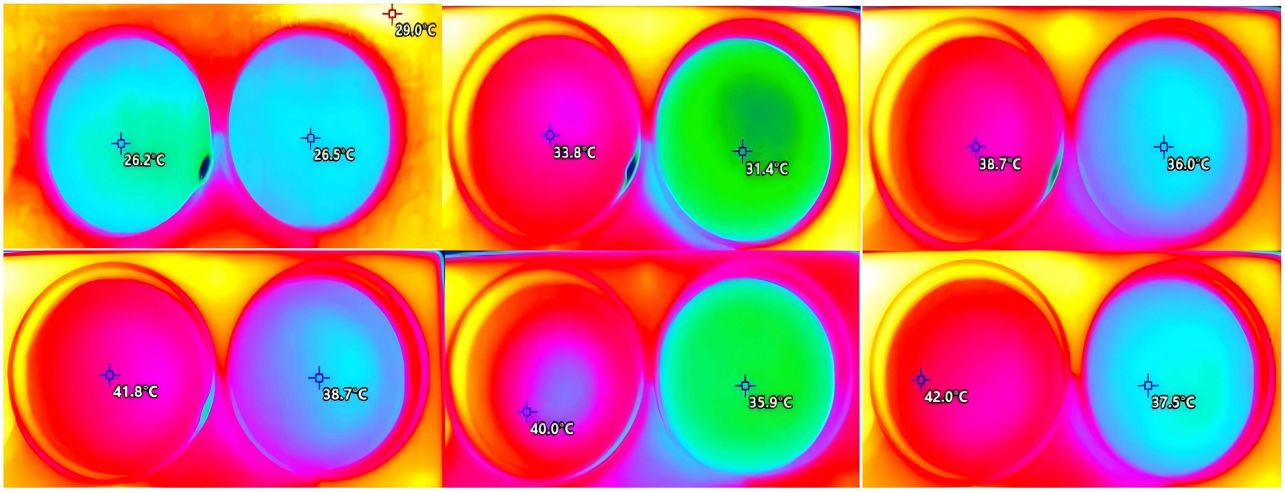

Figure 10 Photothermal performance of the nanocomposite aqueous dispersion under 808 nm NIR laser irradiation. Representative infrared thermal images of pure water (Control) and the $MnFe_2O_4$/ $TiVNbMoC_3$ -RGD nanocomposite dispersion (100 μg/mL) under 808 nm laser irradiation (1.0 W/cm^2) for different durations (0, 5, 10, 15, 20, 25min).

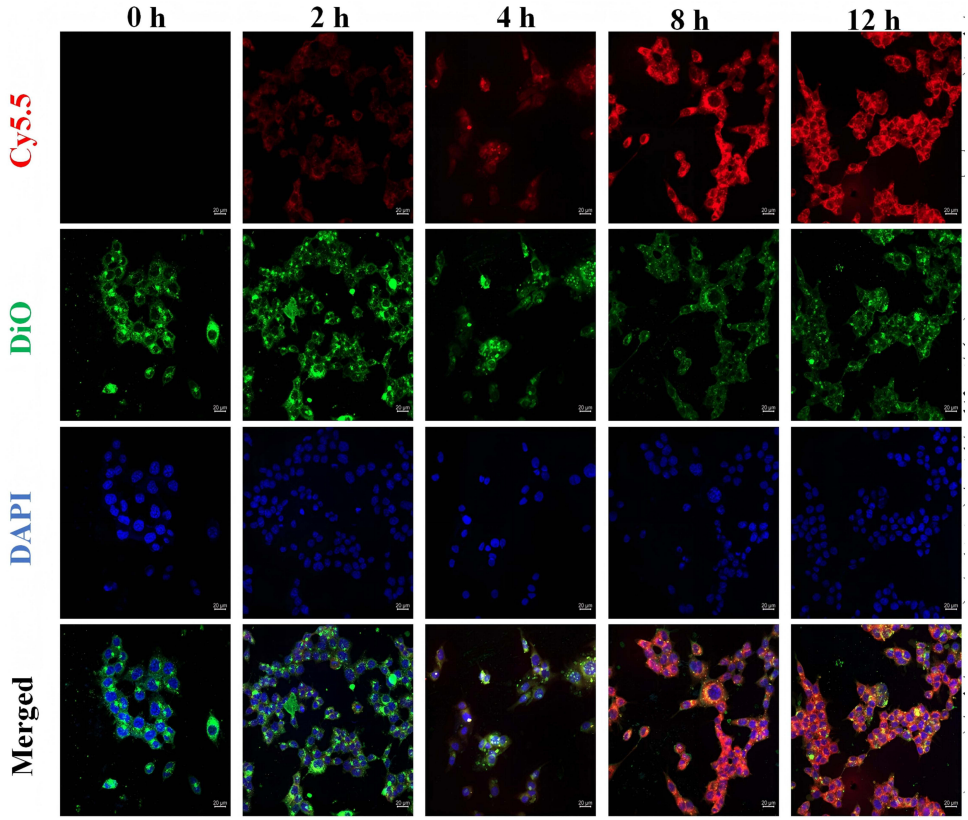

Figure 11 This fluorescence confocal image shows the cellular uptake of the $MnFe_2O_4$/ $TiVNbMoC_3$ -cRGD material at different time points (0, 2, 4, 8, and 12 h). The image is organized into four rows: Cy5.5 (red fluorescence) indicates the distribution of the material within the cells; DiO (green fluorescence) labels the cell membrane; DAPI (blue fluorescence) stains the cell nucleus; and the merged images combine all three channels.

intracellular signal was observed, which showed significant co-localization (yellow) with the DiO-labeled cell membrane (green), confirming effective and time-dependent cellular uptake and internalization. Nuclear morphology, stained with DAPI (blue), remained unchanged.

Antiproliferative Effects

The impact on cell viability and long-term proliferation was assessed. The CCK-8 assay was performed to evaluate the effects of three materials ($TiVNbMoC_3$, $MnFe_2O_4/TiVNbMoC_3$, and $MnFe_2O_4/TiVNbMoC_3$-RGD) on the viability of 5637 bladder cancer cells, which revealed a dose - dependent decrease in cell viability. (Figure 12). While all materials showed comparable effects at lower concentrations (≤25 μg/mL), $MnFe_2O_4$-containing composites exhibited significantly enhanced cytotoxicity at higher doses. At 100 μg/mL, cell viability was reduced to ~10% for both $MnFe_2O_4$ composites, compared to ~40% for $TiVNbMoC_3$ alone.

Additionally, the colony formation assay was carried out to assess the clonogenic capacity of these cells. The colony formation assay further corroborated the superior long-term anti -proliferative effect of the $MnFe_2O_4/TiVNbMoC_3$-RGD nanocomposite (Figure 13). Quantitative analysis showed the average number of colonies decreased from ~160 (control) to 120 ($TiVNbMoC_3$), 70 (doxorubicin, DOX), and only 40 for the $MnFe_2O_4/TiVNbMoC_3$-RGD group, demonstrating its potent suppression of clonogenic survival.

Inhibition of Cell Migration

A scratch wound healing assay evaluated the effect on cell migration (Figure 14). After 48 h, control cells achieved ~95% wound closure. Migration was slightly inhibited by $TiVNbMoC_3$ (~80% closure) and more substantially by DOX (~50% closure). Notably, treatment with $MnFe_2O_4/TiVNbMoC_3$-RGD strongly suppressed migration, resulting in only ~20% wound closure, indicating its potent anti-migratory activity.

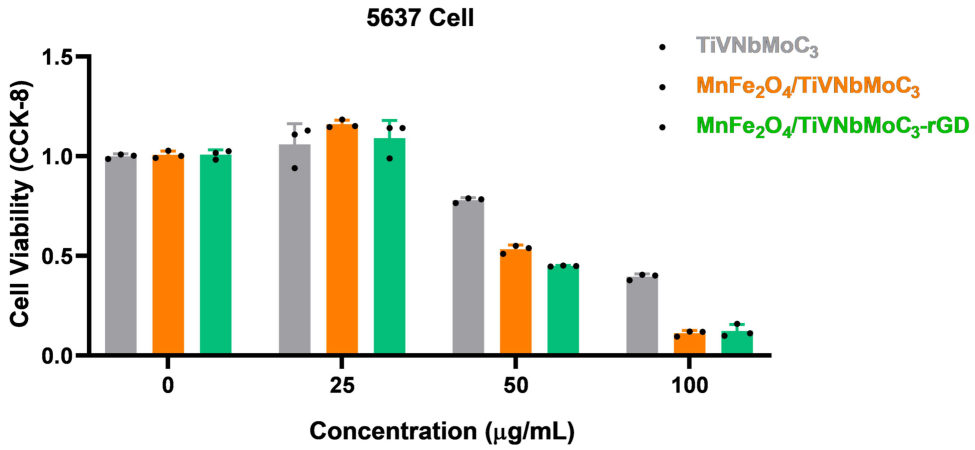

Figure 12 Effects of various nanomaterials on the viability of bladder cancer cells assessed by CCK-8 assay. Cell viability of 5637 cells measured by CCK-8 assay after 48 h treatment (detailed method in Methods 2.2) Data are mean ± SD (n=3). $p < 0.001$ vs control.

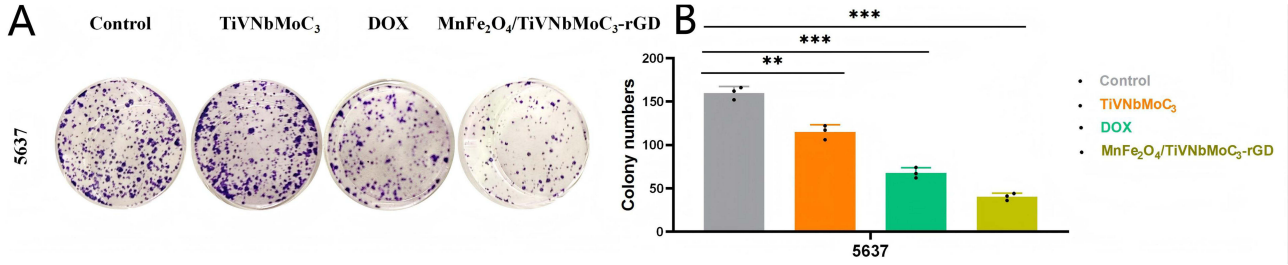

Figure 13 Colony formation assay evaluating the effect of (MnFe2O4/$TiVNbMoC_3$ -RGD) on the clonogenicity of bladder cancer cells. (**A**) Representative images of colonies formed by 5637 cells after treatment with ($MnFe_2O_4/TiVNbMoC_3$ -RGD at 25 ug/mL. (**B**) Statistical analysis of colony numbers. Data are presented as mean ± SD, n=3;**$p < 0.01$, ***$p < 0.001$ vs Control group.

https://doi.org/10.2147/IJN.S597220

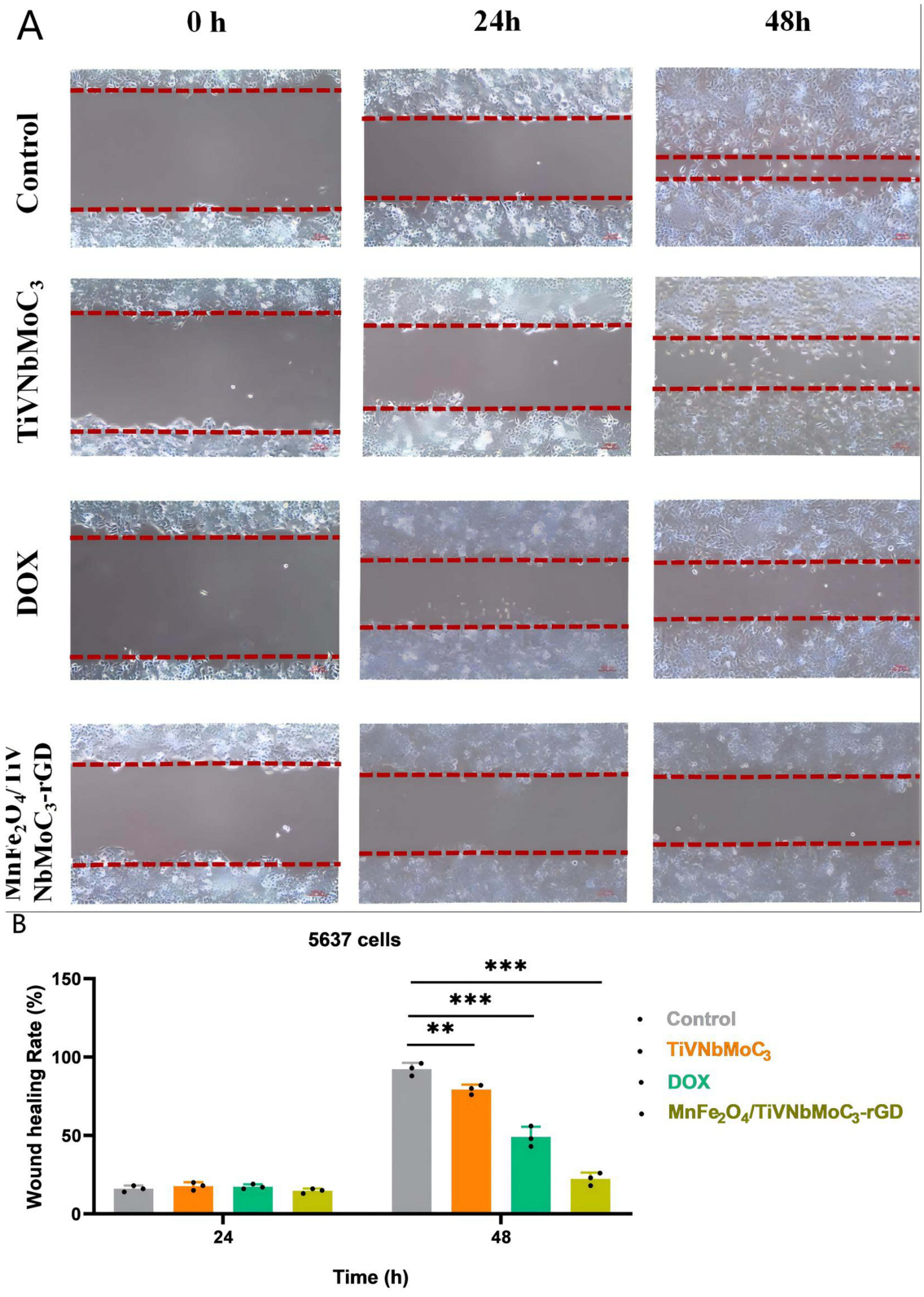

Figure 14 Effects of nanomaterials on the migration ability of bladder cancer cells assessed by scratch wound healing assay. (**A**) Representative microscope images showing wound healing at 0 h and 48 h for 5637 bladder cancer cells treated with PBS (Control), $TiVNbMoC_3$, DOX, and, $MnFe_2O_4$/$TiVNbMoC_3$, and $MnFe_2O_4$/$TiVNbMoC_3$ -RGD (25 ug/mL) for 48 h. Scale bar: 200 um. (**B**) Statistical analysis of wound healing rates calculated from the images. Data are presented as mean ± SD (n=3); $^{**}p < 0.01$,$^{***}p < 0.001$ vs Control group.

https://doi.org/10.2147/IJN.S597220

Induction of Cell Death and Apoptosis

Calcein AM/PI staining visualized live/dead cells (Figure 15). A clear gradient of increasing cytotoxicity was observed: control cells showed dense green fluorescence (live), which moderately decreased in the $TiVNbMoC_3$ and DOX groups with emerging red fluorescence (dead). The $MnFe_2O_4$/ $TiVNbMoC_3$-cRGD group exhibited the most pronounced cytotoxicity, with the weakest green and strongest red fluorescence, indicating favorable cell-killing efficacy over DOX.

Flow cytometry analysis using Annexin V-FITC/PI staining quantified apoptosis. Both control and $TiVNbMoC_3$ groups showed low background apoptosis (<10%). DOX induced moderate apoptosis (~13%) (Figure 16A). In contrast, $MnFe_2O_4$/$TiVNbMoC_3$-RGD group triggered the highest level of apoptosis, reaching ~42%, confirming its potent pro-apoptotic effect (Figure 16B).

Induction of Immunogenic Cell Death (ICD)

Western blot analysis was performed to assess key ICD markers (Figure 17). Compared to the control, HMGB1 and calreticulin (CRT) expression was slightly elevated in the $TiVNbMoC_3$ group and significantly upregulated by DOX. The $MnFe_2O_4$/$TiVNbMoC_3$-cRGD nanocomposite induced the most substantial increase in both proteins, particularly CRT. Equivalent GAPDH levels confirmed consistent loading. These results demonstrate the nanocomposite's efficacy in inducing ICD, characterized by robust CRT exposure and HMGB1 release.

In vivo Antitumor Efficacy

The nanocomposites demonstrated favorable antitumor effects in a bladder cancer xenograft model (Figure 18). Moreover, it exhibited the most potent tumor growth inhibition, with final tumor volume reduced to approximately 1/3 of the control group ($p < 0.001$; Figures 19 and 20), significantly outperforming DOX.

Histopathological and Immunohistochemical Analysis

Tumor tissue analysis further validated the therapeutic outcome. TUNEL staining revealed a marked increase in apoptotic cells in the nanocomposite-treated group compared to all controls (Figure 21). Immunofluorescence for Ki-67 showed

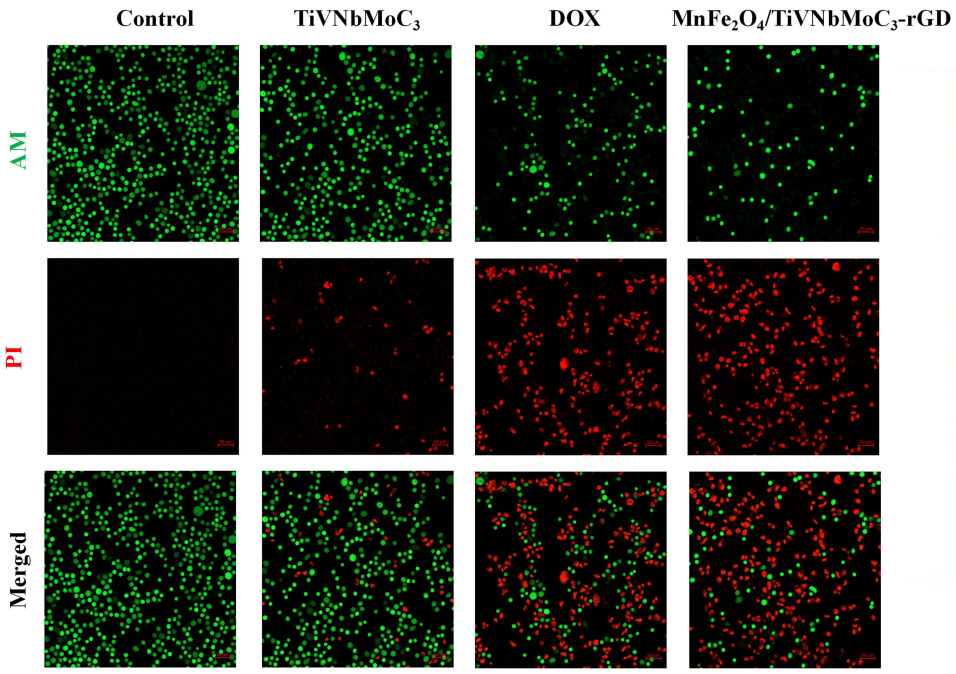

Figure 15 Cytotoxic effect of nanomaterials on bladder cancer cells evaluated by Calcein AM/PI double staining. Representative fluorescence images of 5637 bladder cancer cells after treatment with PBS (Control), $TiVNbMoC_3$, DOX, and $MnFe_2O_4$/$TiVNbMoC_3$ -RGD (50 μg/mL) for 48 h. Live cells are stained green with Calcein AM, and dead cell nuclei are stained red with propidium iodide (PI). Scale bar: 100 μm.

https://doi.org/10.2147/IJN.S597220

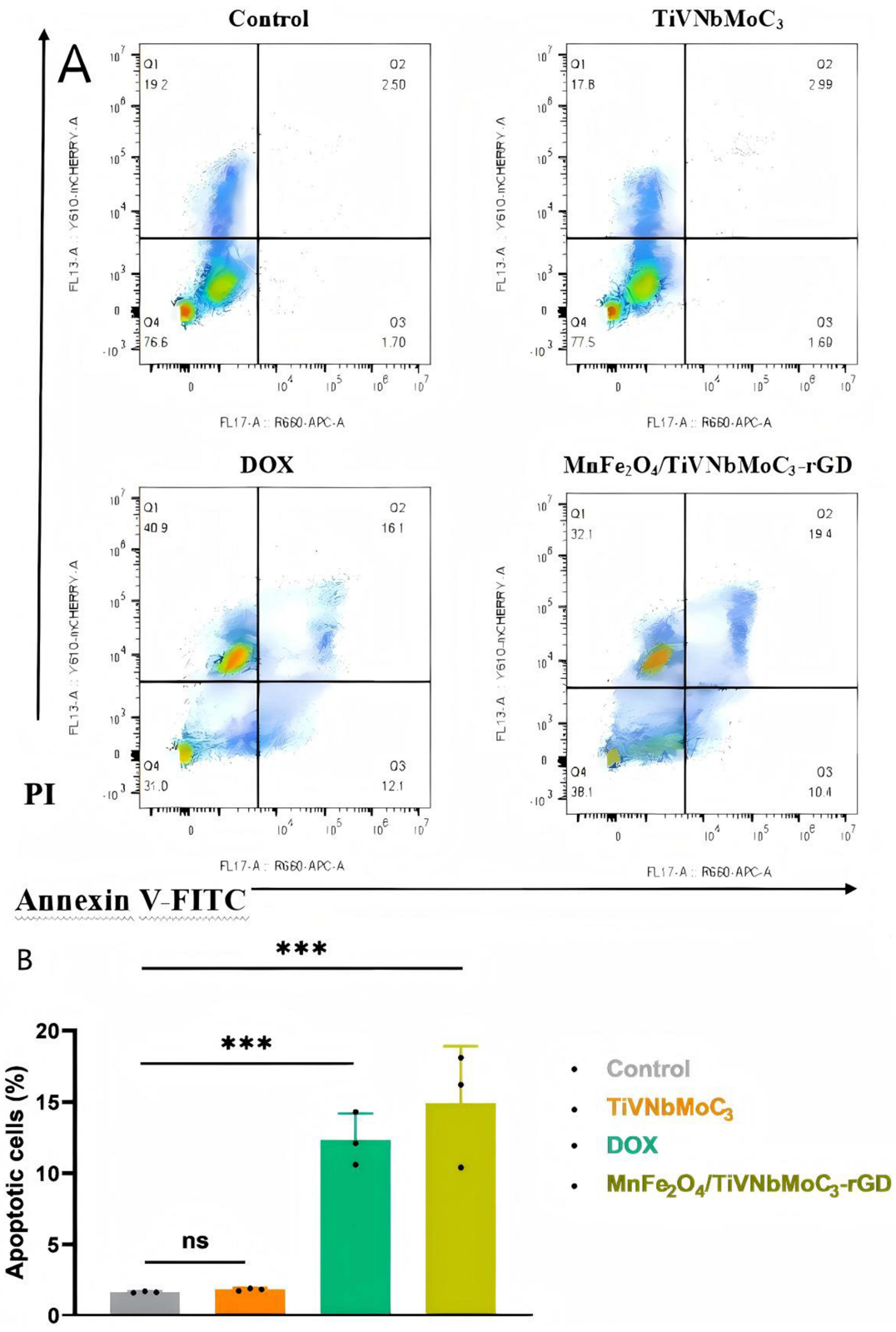

Figure 16 Analysis of cell apoptosis by flow cytometry using Annexin V-APC/PI staining.(**A**) Representative flow cytometry scatter plots showing apoptosis of 5637 bladder cancer cells treated with PBS (Control), $TiVNbMoC_3$, DOX, and $MnFe_2O_4$/ $TiVNbMoC_3$-cRGD (25 μg/mL) for 48 h. The lower left quadrant (Annexin V^-/PI^-) represents live cells, lower right quadrant (Annexin V^+/PI^-) early apoptotic cells, and upper right quadrant (Annexin V^+/PI^+) late apoptotic/ necrotic cells.(**B**) Quantitative analysis of total apoptotic cells (early + late) from three independent experiments. The control and $TiVNbMoC_3$ groups showed low background apoptosis (<10%). DOX induced moderate apoptosis (~13%). The $MnFe_2O_4$/ $TiVNbMoC_3$-cRGD nano -composite triggered the highest level of apoptosis (~42%), indicating its potent pro-apoptotic effect. Data are presented as mean ± SD (n = 3). ns (not significant) indicates no statistically significant difference between the indicated groups (eg, Control vs $TiVNbMoC_3$),***$p < 0.001$ indicates a statistically significant difference compared to the control group (one way ANOVA with Tukey's post-hoc test).

 https://doi.org/10.2147/IJN.S597220

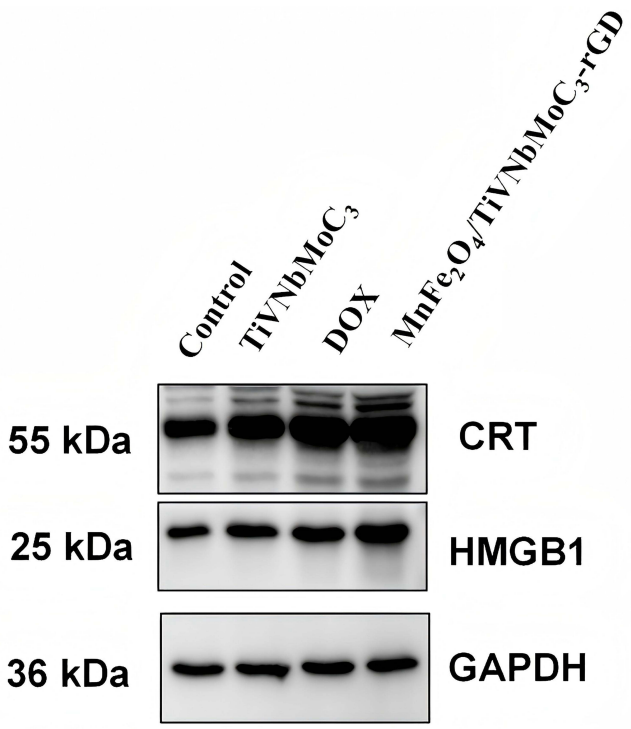

Figure 17 Western blot analysis shows the effect of different treatment groups on the expression of immunogenic cell death markers in bladder cancer cells.

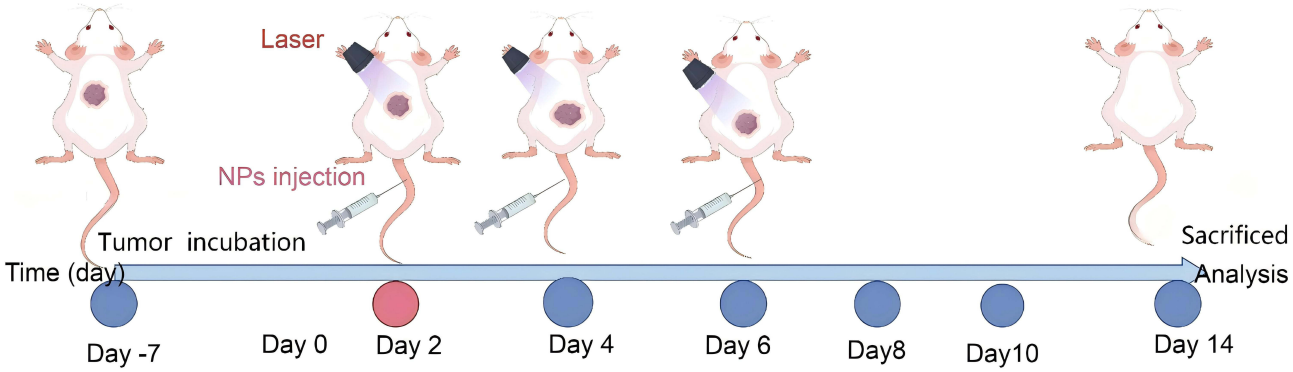

Figure 18 Schematic illustration of tumor therapeutic protocols.

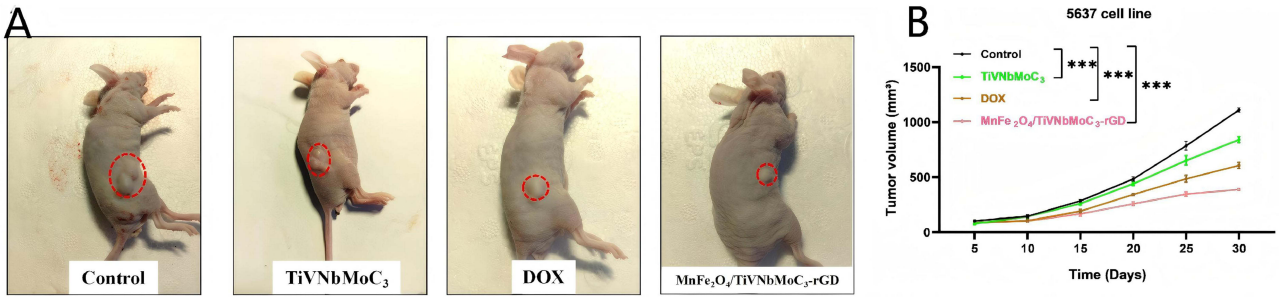

Figure 19 (**A**) Bladder xenograft tumor mouse models of different groups and (**B**) Statistical analysis of tumor growth curves measured after 14 days of treatment. Data are presented as mean ± SD (n=5),***p < 0.001 vs Control group.

https://doi.org/10.2147/IJN.S597220

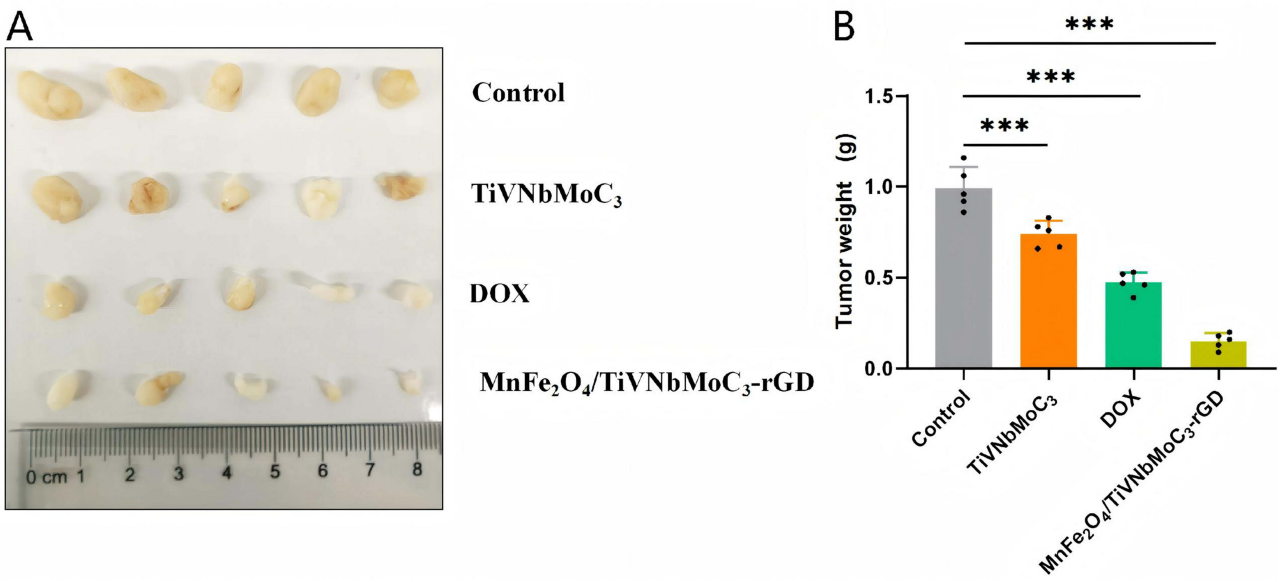

Figure 20 Inhibitory effects on tumor growth by different drug treatment groups. (**A**) Tumor volume curves over time in mice treated with PBS (Control), $TiVNbMoC_3$, DOX, and $MnFe_2O_4$/ $TiVNbMoC_3$-cRGD (25 μg/mL) for 14 days. (**B**) Representative photographs of excised tumors at the end of treatment. Statistical analysis of tumor weights. Data are presented as mean ± SD (n=5); ***p < 0.001 vs Control group.

a significant reduction in proliferating cells, and this reduction was supported by a decreased nuclear-cytoplasmic ratio in DAPI-stained sections (Figure 22). H&E staining confirmed the most substantial tumor tissue damage -including structural disruption, vacuolation, and necrosis—following nanocomposite treatment (Figure 23).

Biosafety and Biocompatibility Assessment

A hemolysis assay indicated concentration-dependent effects, with negligible hemolysis (<5%) at concentrations below 50 μg/mL and a critical threshold near 100 μg/mL (Figure 24). Histopathological examination of major organs (heart, liver, spleen, lungs, kidneys) from treated mice showed no obvious lesions or damage compared to controls, confirming the appreciable in vivo biocompatibility of the nanocomposite (Figure 25).

Statistical Analysis

SPSS version 22.0 was used for statistical analyses. One-way analysis of variance (ANOVA) or *t* test for multiple comparisons was used for statistical analysis. All data were expressed as mean±standard deviation (SD). Statistical significance was set at $p<0.05$, $p<0.01$ as indicated in the figures.

Discussion

The continuous advancement of nanotechnology, combined with single-modality therapies, has established Schottky junction nanomaterials as promising agents for the multimodal treatment of bladder cancer.[18] The heterostructure of Schottky junction nanomaterials efficiently separates and transports electron-hole pairs upon photo excitation,[19] leading to markedly enhanced ROS production.[20] This photocatalytic activity can be leveraged to induce ICD in bladder cancer cells,[21] while the integrated PTT function provides a dual-action therapeutic strategy that targets malignancies with reduced off-target damage. Pan et al[22] constructed a multifunctional nanodiagnostic probe by combining bladder cancer-targeting cyclopeptides, chemotherapeutic drugs, and photosensitizers for PDT, which integrated simultaneous fluorescence imaging, PDT and CDT, providing a comprehensive approach to bladder cancer management. Therefore, employing multimodal treatment, there is potential to overcome the limitations of biologically and clinically heterogeneous and effectively combat tumor drug resistance and immune evasion.[23]

Building on this foundation, we successfully fabricated a metal-semiconductor nanocomposite, $MnFe_2O_4$ /$TiVNbMoC_3$-cRGD MXenes. Comprehensive characterization (STEM, EDX, XRD, DLS, XPS) verified its structural

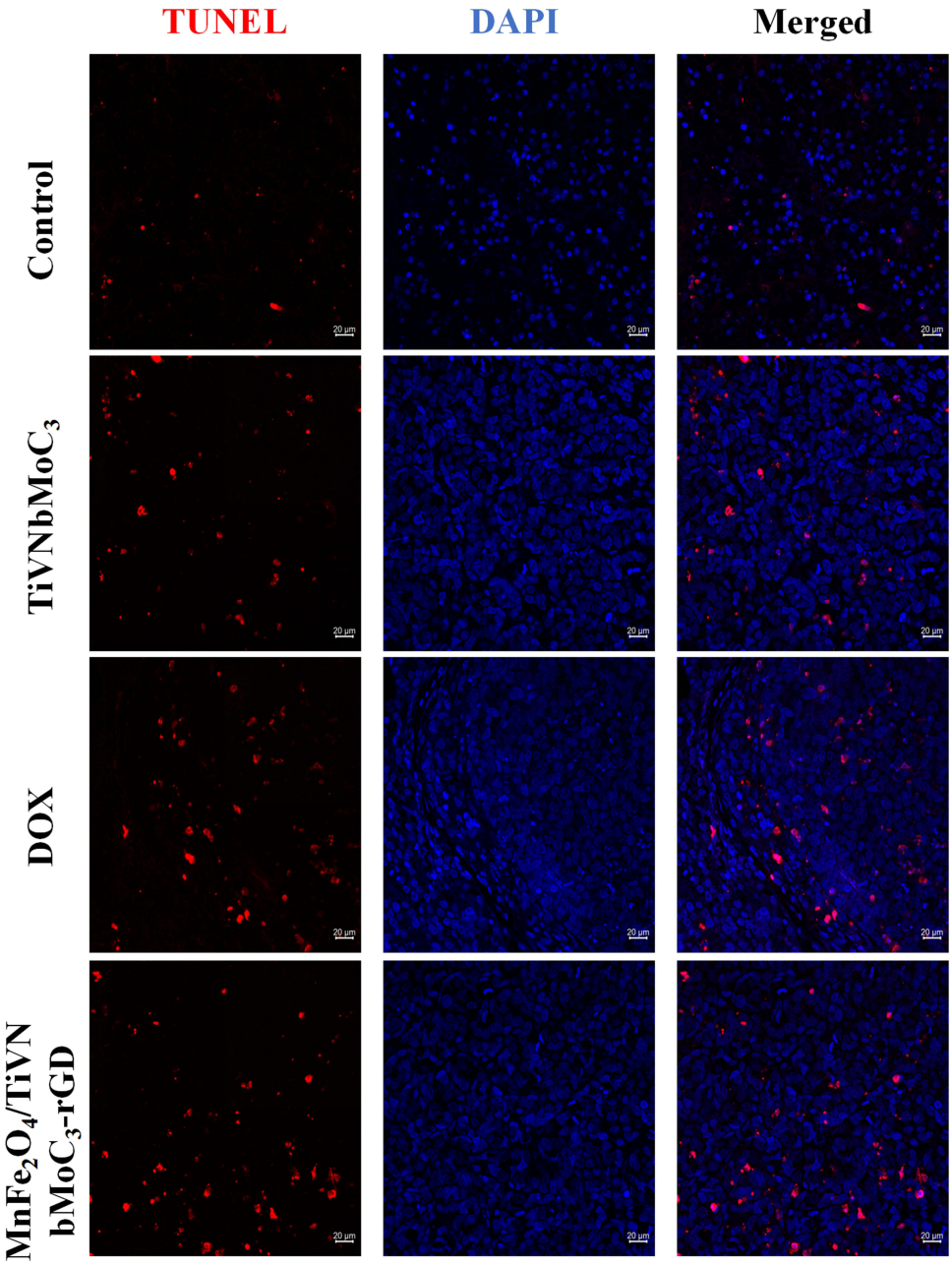

Figure 21 Analysis of nanomaterial-induced apoptosis in tumor tissues via TUNEL assay Schematic of the staining protocol: after deparaffinization and permeabilization, DNA strand breaks were labeled (red, 520 nm) and nuclei were counterstained with DAPI (blue, 460 nm).

integrity and the homogeneous distribution of constituent elements (Ti, V, Nb, C, O).[24,25] The material possesses an expanded active surface area, which promotes structural uniformity. Meanwhile, the intimate interfacial contact between the $TiVNbMoC_3$ and $MnFe_2O_4$ phases facilitates efficient charge transfer, which is a critical feature underlying its synergistic photodynamic and photothermal capabilities. Furthermore, UV-vis spectroscopy confirmed that incorporating $MnFe_2O_4$ substantially modulates the composite's optical properties, resulting in broadened light absorption across an extended wavelength range and thereby enhancing its suitability for photo-mediated therapies.[26]

Rationale for MXene selection. Why MXene? The current study designed a $MnFe_2O_4$/ $TiVNbMoC_3$-RGD Schottky junction, leveraging the inherent advantages of MXenes as a 2D transition metal carbide family: (1) broad NIR absorption due to localized surface plasmon resonance, enabling efficient photothermal heating under 808 nm laser without extra plasmonic nanoparticles;[27] (2) Schottky junction formation when interfaced with $MnFe_2O_4$, creating

https://doi.org/10.2147/IJN.S597220

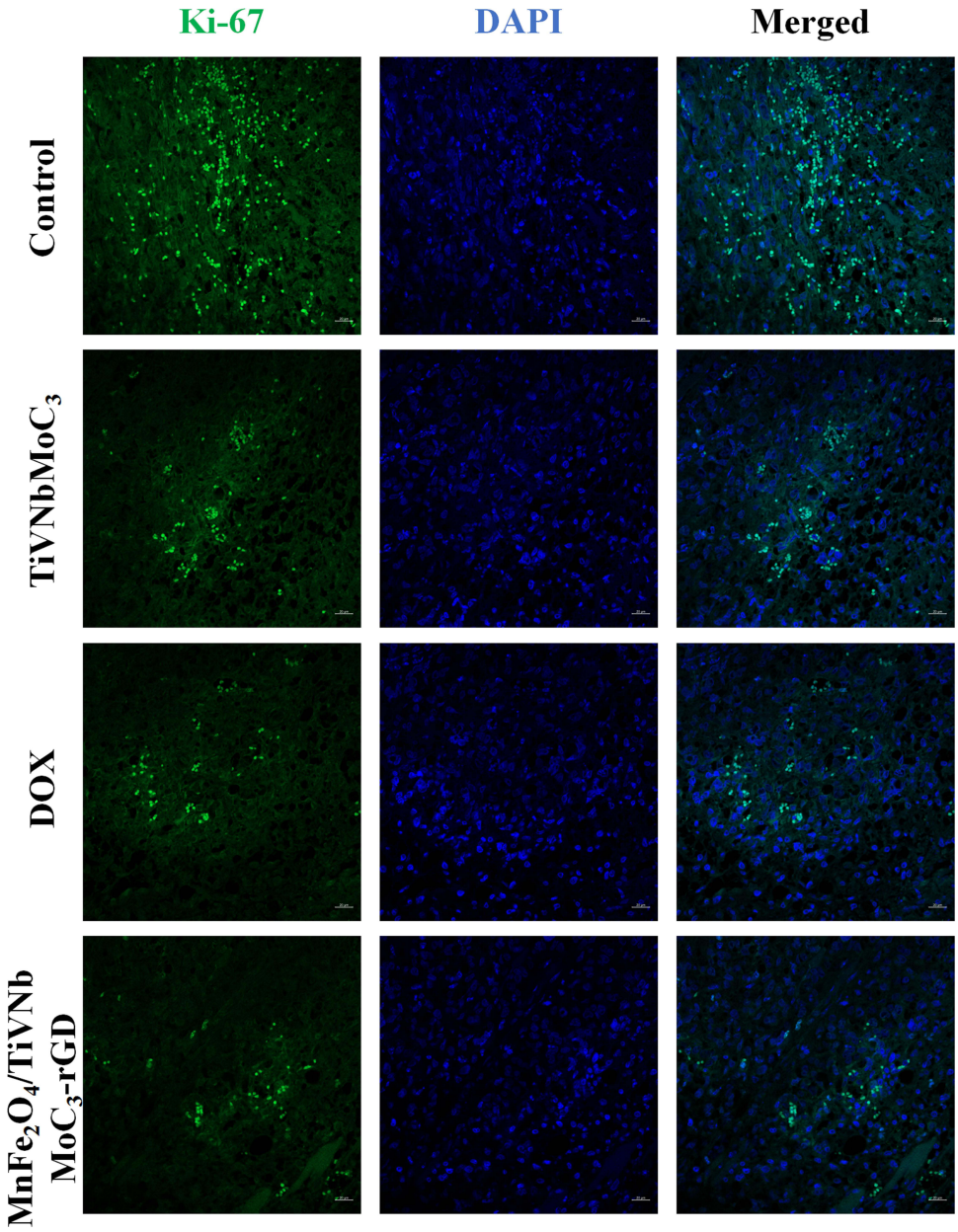

Figure 22 Assessment of tumor cell proliferation by Ki-67 immunofluorescence staining.

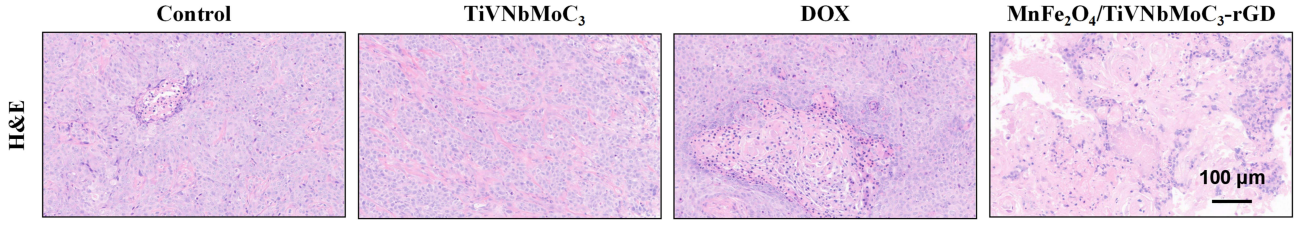

Figure 23 H&E staining for histopathological analysis.

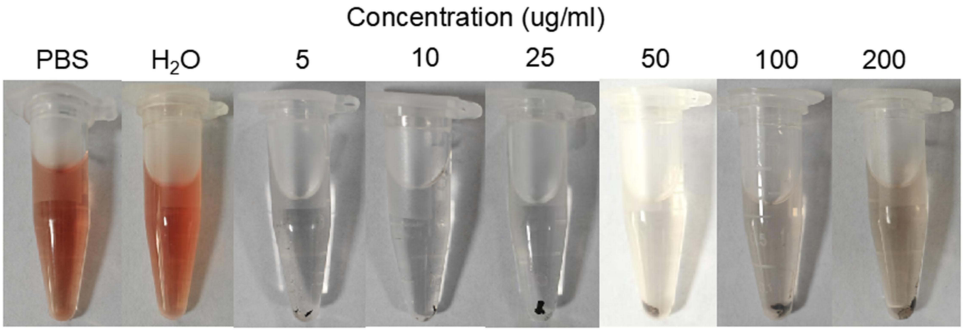

Figure 24 Different concentrations of nanomaterials in hemolysis assay.

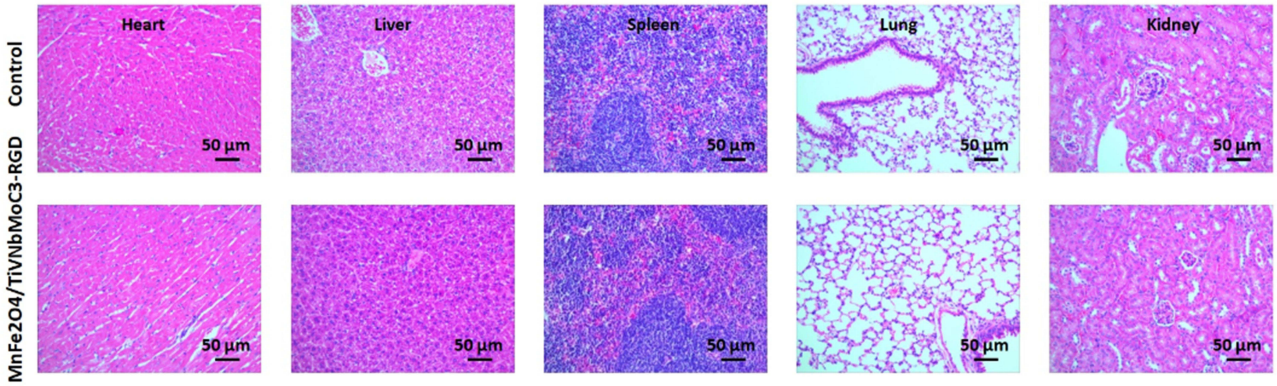

Figure 25 Histological analysis of major organs of healthy mice with the treatment of MnFe2O4/TiVNbMoC3-rGD.

a built-in electric field that separates electron-hole pairs and suppresses recombination, thereby boosting ROS generation for PDT/CDT;[28] (3) abundant surface groups (–OH, –O, –F) conferring good aqueous dispersibility, facile ligand conjugation (eg, cRGD), and favorable biocompatibility (minimal hemolysis, no organ toxicity at therapeutic doses);[29] and (4) high surface area allowing dense $MnFe_2O_4$ loading for synergistic PTT/PDT.

Specifically, the quinary MXene $TiVNbMoC_3$ was chosen over conventional binary or ternary MXenes (eg, Ti_3C_2, Nb_2C) due to its high compositional entropy. This high-entropy configuration has been reported to confer even broader optical absorption across the UV-vis-NIR region, enhanced colloidal stability, and improved resistance to oxidation compared to lower entropy MXenes.[30] A preliminary screening also indicated that $TiVNbMoC_3$ exhibits a higher photothermal conversion efficiency under 808 nm laser irradiation than Ti_3C_2, justifying the added synthetic complexity.[31]

Most significantly, this nanocomposite effectively triggered ICD in bladder cancer cells. This effect was demonstrated by a robust increase in ROS and the upregulation of classical ICD markers-specifically, the surface exposure of CRT and the extracellular release of HMGB1, as confirmed by Western blot analysis.[32,33] This finding aligns well with the observed in vivo antitumor efficacy and suppression of colony formation. Furthermore, the migration assay (Figure 14) showed that nanocomposite treatment reduced wound closure to only ~20% (compared to ~95% in controls), confirming its potent anti-invasive activity. Given that bladder cancer progression to muscle-invasive disease critically depends on tumor cell migration and invasion, this anti-migratory effect is clinically relevant. Although we did not directly assess metastasis in vivo, the marked reduction in wound closure suggests that this Schottky junction platform may also suppress metastatic dissemination. Future studies using orthotopic or experimental metastasis models (eg, tail vein injection) are warranted to confirm this.

https://doi.org/10.2147/IJN.S597220

Thus, the combination of anti-migratory activity and ICD-induced adaptive immunity offers a dual mechanism that could potentially reduce both local recurrence and systemic spread—two major clinical challenges in bladder cancer management. Together with results from the colony formation and apoptosis assays, these damage-associated molecular patterns indicate that the nanocomposite can elicit a potent antitumor immune response. Furthermore, in vivo studies demonstrated favorable antitumor effects in a preclinical murine model compared with single-agent DOX chemotherapy, while showing minimal toxicity to vital organs. Collectively, these findings confirm that our platform has dual mode therapeutic action through combined PDT and PTT therapy. Moreover, in vivo studies demonstrated favorable anti-tumor effects in a preclinical murine model compared to single-agent DOX chemotherapy, with minimal toxicity to vital organs, suggesting its potential for further translational investigation. By simultaneously inhibiting migration and triggering ICD, this targeted nanocomposite addresses not only primary tumor growth but also the risk of progression and metastasis, thereby aligning with the urgent clinical need for more comprehensive bladder cancer therapies.

Nevertheless, this study has certain limitations. First, While CRT and HMGB1 confirm ICD, the upstream signaling pathways (eg, ER stress or caspase-dependent mechanisms) were not examined. Emerging evidence has established that therapy-induced ER stress can elicit ICD through the PERK–eIF2α–ATF4–CHOP pathway,[34] and that caspase activation plays a dual role in regulating ICD hallmark factors.[35] Furthermore, the immunogenicity of the nanocomposite in vivo (eg, T-cell infiltration or cytokine profiling) warrants further study. Nanosphere-mediated cytokine modulation has been shown to increase pro-inflammatory cytokines such as IFN-γ, IL-6, and TNF-α,[36] and enhanced $CD8^+$ T cell infiltration has been reported as a critical readout of ICD-driven antitumor immunity.[37] Similarly, an FGFR3 -targeting antibody drug conjugate developed by Shu Cui et al[38] induced bladder cancer cell apoptosis via activation of the cGAS-STING pathway. These reports suggest that further investigation into the immunomodulatory or pathway-specific mechanisms of our system could help optimize its therapeutic efficacy. Second, the current work focuses on the photothermal and photodynamic properties of the material. However, environmental factors like solution pH and temperature may affect its stability and function. These aspects have not been systematically studied and will be investigated in future research. Third, only a single cell line was employed in this study. Other cell types, such as T24 or UM-UC-3, warrant further inclusion in subsequent research.

Moreover, one limitation of this study is the lack of a dedicated "Laser Only" control group. While previous reports using identical 808 nm laser parameters on bladder cancer cells have shown negligible cytotoxicity and no significant tumor growth inhibition in the absence of a PTT agent,[39] we cannot completely rule out a minor contribution from direct laser heating. However, the dramatic difference in anti-tumor efficacy between the nanocomposite treated group and the PBS control, together with the minimal temperature rise observed in preliminary thermographic measurements without the nanocomposite ($\Delta T < 4$ °C), strongly suggests that the observed cell death is primarily driven by the nanocomposite's PTT and PDT effects.[40] Future studies will incorporate a "Laser Only" arm to definitively separate the thermal contribution.

Conclusion

This MXene-based Schottky junction nanocomposite $MnFe_2O_4$/TiVNbMoC_3-cRGD represents a promising targeted platform for dual-modal photothermal/photodynamic therapy combined with immune activation in bladder cancer, warranting further translational investigation.

Abbreviations

PDT, Photodynamic Therapy; PTT, Photothermal Therapy; ROS, Reactive Oxygen Species; ICD, Immunogenic Cell Death; NIR, Near-infrared; STEM, Scanning transmission electron microscopy; EDX, Energy dispersive X ray spectroscopy; XPS, X ray photoelectron spectroscopy; ATP, Adenosine triphosphate; CRT, Calreticulin; ICD, Immunogenic cell death; HMGB1, High-mobility group box 1.

Author Contributions

We gratefully acknowledge all authors making great contributions to the article. All authors made a significant contribution to the work reported, whether that is in the conception, study design, execution, acquisition of data, analysis

and interpretation, or in all these areas; took part in drafting, revising or critically reviewing the article; gave final approval of the version to be published; have agreed on the journal to which the article has been submitted; and agree to be accountable for all aspects of the work.

Funding

The study was supported by the General project of basic scientific research of Nantong Health Commission (MSZ2024032), Medical Research Project of Nantong Health Commission (MS2024032) and (MSZ2024099).

Disclosure

The authors declare that they have no competing interests.

References

1. Siegel RL, Miller KD, Fuchs HE, Jemal A. Cancer statistics, 2022. *CA Cancer J Clin*. 2022;72(1):7–33. doi:10.3322/caac.21708
2. Wang F, Dong X, Yang F, Xing N. Comparative analysis of differentially mutated genes in non-muscle and muscle-invasive bladder cancer in the chinese population by whole exome sequencing. *Front Genet*. 2022;13:831146. doi:10.3389/fgene.2022.831146
3. Heer R, Lewis R, Duncan A, et al. Photodynamic versus white-light-guided resection of first-diagnosis non-muscle-invasive bladder cancer: PHOTO RCT. *Health Technol Assess*. 2022;26(40):1–144. doi:10.3310/PLPU1526
4. Yang Z, Yang X, Guo Y, Kawasaki H. A review on gold nanoclusters for cancer phototherapy. *ACS Appl Bio Mater*. 2023;6(11):4504–4517. doi:10.1021/acsabm.3c00518
5. Nadeem F, Zhang H, Tahir N, et al. Advances in the catalyzed photo-fermentative biohydrogen production through photo nanocatalysts with the potential of selectivity, and customization. *Bioresour Technol*. 2023;382:129221. doi:10.1016/j.biortech.2023.129221
6. Wu W, Pu Y, Shi J. Nanomedicine-enabled chemotherapy-based synergetic cancer treatments. *J Nanobiotechnology*. 2022;20(1):4. doi:10.1186/s12951-021-01181-z
7. Fan W, Yung B, Huang P, Chen X. Nanotechnology for multimodal synergistic cancer therapy. *Chem Rev*. 2017;117(22):13566–13638. doi:10.1021/acs.chemrev.7b00258
8. Chen WH, Yu KJ, Jhou JW, et al. Glucose/glutathione co-triggered tumor hypoxia relief and chemodynamic therapy to enhance photothermal therapy in bladder cancer. *ACS Appl Bio Mater*. 2021;4(10):7485–7496. doi:10.1021/acsabm.1c00741
9. Wang Y, Liu S, Li Q, et al. Schottky barrier heights in two-dimensional field-effect transistors: from theory to experiment. *Rep Prog Phys*. 2021;84(5). doi:10.1088/1361-6633/abf1d4
10. An K, Hu J, Wang J. Schottky-barrier-free plasmonic photocatalysts. *Phys Chem Chem Phys*. 2023;25(29):19358–19370. doi:10.1039/d3cp01425h
11. Vivona M, Giannazzo F, Roccaforte F. Materials and processes for Schottky contacts on silicon carbide. *Materials (Basel)*. 2021;15(1):298. doi:10.3390/ma15010298
12. Ma C, Cheng Z, Tan H, et al. Nanomaterials: leading immunogenic cell death-based cancer therapies. *Front Immunol*. 2024;15:1447817. doi:10.3389/fimmu.2024.1447817
13. Ou M, Lin C, Wang Y, et al. Heterojunction engineered bioactive chlorella for cascade promoted cancer therapy. *J Control Release*. 2022;345:755–769. doi:10.1016/j.jconrel.2022.03.059
14. Chang Y, Cheng Y, Feng Y, et al. Resonance energy transfer-promoted photothermal and photodynamic performance of gold-copper sulfide yolk-shell nanoparticles for chemophototherapy of cancer. *Nano Lett*. 2018;18(2):886–897. doi:10.1021/acs.nanolett.7b04162
15. Chen H, Qi Y, Yang C, et al. Heterogeneous MXene hybrid-oriented exosome isolation and metabolic profiling for early screening, subtyping and follow-up evaluation of bladder cancer. *ACS Nano*. 2023;17(23):23924–23935. doi:10.1021/acsnano.3c08391
16. Zhao Y, Liu J, He M, et al. Platinum-titania schottky junction as nanosonosensitizer, glucose scavenger, and tumor microenvironment-modulator for promoted cancer treatment. *ACS Nano*. 2022;16(8):12118–12133. doi:10.1021/acsnano.2c02540
17. Weiss J, Pham NA, Pintilie M, et al. Optimizing drug response study design in patient-derived tumor xenografts. *Cancer Inform*. 2022;21:11769351221136056. doi:10.1177/11769351221136056
18. Duan F, Jia Q, Liang G, et al. Schottky junction nanozyme based on mn-bridged co-phthalocyanines and Ti3C2Tx nanosheets boosts integrative type I and II photosensitization for multimodal cancer therapy. *ACS Nano*. 2023;17(12):11290–11308. doi:10.1021/acsnano.2c12270
19. Wang X, Gao S, Ma J. Schottky barrier effect on plasmon-induced charge transfer. *Nanoscale*. 2023;15(4):1754–1762. doi:10.1039/d2nr05937a
20. Xu K, Gu D, Zhang Y, Su Q, Chen J, Gu Z. Engineering Schottky junction nanocatalysts for enhanced charge carrier separation and synergistic PDT/PTT/CDT in bladder cancer therapy. *ACS Biomater Sci Eng*. 2025;11(9):5228–5236. doi:10.1021/acsbiomaterials.5c00960
21. Reinhold A, Glasow A, Nürnberger S, et al. Ionizing radiation and photodynamic therapy lead to multimodal tumor cell death, synergistic cytotoxicity and immune cell invasion in human bladder cancer organoids. *Photodiagnosis Photodyn Ther*. 2025;51:104459. doi:10.1016/j.pdpdt.2024.104459
22. Lin TY, Li Y, Liu Q, et al. Novel theranostic nanoporphyrins for photodynamic diagnosis and trimodal therapy for bladder cancer. *Biomaterials*. 2016;104:339–351. doi:10.1016/j.biomaterials.2016.07.026
23. Sun Y, Wang H, Yang Y, et al. Schottky barrier-based built-in electric field for enhanced tumor photodynamic therapy. *ACS Appl Mater Interfaces*. 2024;16(13):15916–15930. doi:10.1021/acsami.4c00018
24. Cha E, Chung H, Jang J, Lee J, Lee E, Ye JC. Low-dose sparse-view HAADF-STEM-EDX tomography of nanocrystals using unsupervised deep learning. *ACS Nano*. 2022;16(7):10314–10326. doi:10.1021/acsnano.2c00168
25. Predoi D, Ciobanu SC, Iconaru SL, et al. New physico-chemical analysis of magnesium-doped hydroxyapatite in dextran matrix nanocomposites. *Polymers (Basel)*. 2023;16(1):125. doi:10.3390/polym16010125

26. Zou Q, Bao J, Yan X. Functional nanomaterials based on self-assembly of endogenic NIR-absorbing pigments for diagnostic and therapeutic applications. *Small Methods*. 2022;6(4):e2101359. doi:10.1002/smtd.202101359
27. Liu Y, Wu X, Ye S, et al. MXene Ti3CNTx for near-infrared plasmonics and high broadband absorption. *Opt Lett*. 2025;50(21):6867–6870. doi:10.1364/OL.576727
28. Meng J, Xie S, Zhang Z, et al. pH-triggered Schottky heterojunctions for NIR-II-activated and tumor-specific pyroelectrodynamic and photothermal therapy. *J Colloid Interface Sci*. 2026;702(Pt 1):138919. doi:10.1016/j.jcis.2025.138919
29. Sun H, Jin Y, Alam F. Review: the application of MXene in thermal energy storage materials for efficient solar energy utilization. *Materials (Basel)*. 2025;18(12):2839. doi:10.3390/ma18122839
30. Yousuf M, Liu X, Schroeder CW, Tjioe J, Liu Y, Wu Y. Rise of high-entropy MXenes in electrocatalysis for sustainable energy conversion. *Chem Commun (Camb)*. 2026;62(40):10100–10131. doi:10.1039/d6cc00413j
31. Zou Q, Qiu A, He Y, et al. Fabrication of polydopamine-coated high-entropy MXene nanosheets for targeted photothermal anticancer therapy. *Adv Sci (Weinh)*. 2025;12(7):e2410537. doi:10.1002/advs.202410537
32. Wu PJ, Chiou HL, Hsieh YH, et al. Induction of immunogenic cell death effect of licoricidin in cervical cancer cells by enhancing endoplasmic reticulum stress-mediated high mobility group box 1 expression. *Environ Toxicol*. 2023;38(7):1641–1650. doi:10.1002/tox.23793
33. Hejazi MS, Jafari S, Montazersaheb S, et al. Annexin A1, calreticulin and high mobility group box 1 are elevated in secondary progressive multiple sclerosis: does immunogenic cell death occur in multiple sclerosis? *Bioimpacts*. 2024;15:30264. doi:10.34172/bi.30264
34. Shang K, Montesdeoca N, Zhang H, et al. Cobalt(III) prodrug-based nanomedicine for inducing immunogenic cell death and enhancing chemo-immunotherapy. *J Control Release*. 2024;373:493–506. doi:10.1016/j.jconrel.2024.07.042
35. Eek Mariampillai A, Hauge S, Kongsrud K, Syljuåsen RG. Immunogenic cell death after combined treatment with radiation and ATR inhibitors is dually regulated by apoptotic caspases. *Front Immunol*. 2023;14:1138920. doi:10.3389/fimmu.2023.1138920
36. Lacinski RA, Dziadowicz SA, Stewart A, et al. Nanosphere pharmacodynamics improves safety of immunostimulatory cytokine therapy. *iScience*. 2024;27(2):108836. doi:10.1016/j.isci.2024.108836
37. Li Y, Chen J, Xia Q, et al. Photothermal Fe3O4 nanoparticles induced immunogenic ferroptosis for synergistic colorectal cancer therapy. *J Nanobiotechnology*. 2024;22(1):630. doi:10.1186/s12951-024-02909-3
38. Cui S, Luo X, Fan G, et al. A novel FGFR3-targeting antibody-drug conjugate induces tumor cell apoptosis through the cGAS-STING pathway in bladder cancer. *Adv Sci (Weinh)*. 2025;13(4):e09933. doi:10.1002/advs.202509933
39. Chen H, Zhao X, Halimov A, et al. Phototheranostic zinc porphyrin nanoparticles triggered by an 808 nm laser: NIR-II fluorescence/photoacoustic imaging-guided combined photothermal/photodynamic/NO therapy. *Bioconjug Chem*. 2025;36(4):838–845. doi:10.1021/acs.bioconjchem.5c00086
40. Ni W, Li M, Cui J, et al. 808nm light triggered black TiO2 nanoparticles for killing of bladder cancer cells. *Mater Sci Eng C Mater Biol Appl*. 2017;81:252–260. doi:10.1016/j.msec.2017.08.020